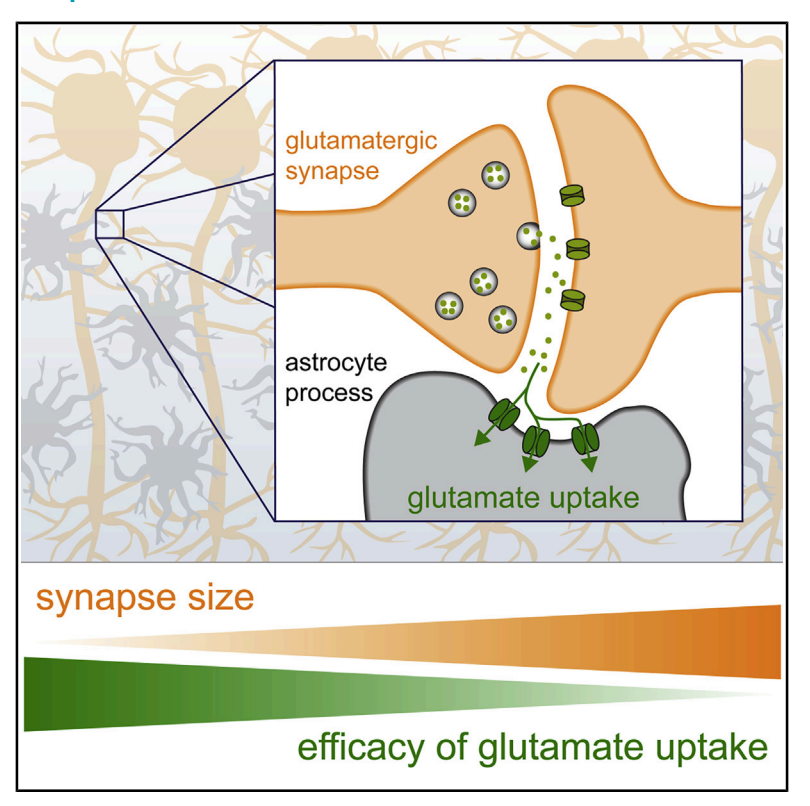
# **Local Efficacy of Glutamate Uptake Decreases with Synapse Size**

## **Graphical Abstract**



#### **Authors**

Michel K. Herde, Kirsten Bohmbach, Cátia Domingos, ..., Dirk Dietrich, Martin K. Schwarz, Christian Henneberger

### Correspondence

christian.henneberger@uni-bonn.de

#### In Brief

Herde et al. demonstrate a dependence of the local efficacy of glutamate uptake at glutamatergic synapses on spine size. As predicted by the relative astrocytic coverage of spines, extracellular glutamate transients and Ca<sup>2+</sup> entry through glutamate receptors are less strongly controlled by glutamate uptake at large than at small spines.

## **Highlights**

- Relative astrocytic coverage of glutamatergic spines decreases with spine size
- Control of perisynaptic glutamate transients by uptake decreases with spine size
- Control of receptor-mediated Ca<sup>2+</sup> entry by uptake decreases with spine size
- Accordingly, small spines are better shielded from invading glutamate







## **Article**

# Local Efficacy of Glutamate Uptake Decreases with Synapse Size

Michel K. Herde, Kirsten Bohmbach, Cátia Domingos, Natascha Vana, Joanna A. Komorowska-Müller, Stefan Passlick, Inna Schwarz, Colin J. Jackson, Dirk Dietrich, Martin K. Schwarz, and Christian Henneberger, 5,6,7,\*

<sup>1</sup>Institute of Cellular Neurosciences, Medical Faculty, University of Bonn, Bonn, Germany

#### **SUMMARY**

Synaptically released glutamate is largely cleared by glutamate transporters localized on perisynaptic astrocyte processes. Therefore, the substantial variability of astrocyte coverage of individual hippocampal synapses implies that the efficacy of local glutamate uptake and thus the spatial fidelity of synaptic transmission is synapse dependent. By visualization of sub-diffraction-limit perisynaptic astrocytic processes and adjacent postsynaptic spines, we show that, relative to their size, small spines display a stronger coverage by astroglial transporters than bigger neighboring spines. Similarly, glutamate transients evoked by synaptic stimulation are more sensitive to pharmacological inhibition of glutamate uptake at smaller spines, whose high-affinity N-methyl-D-aspartate receptors (NMDARs) are better shielded from remotely released glutamate. At small spines, glutamate-induced and NMDAR-dependent Ca<sup>2+</sup> entry is also more strongly increased by uptake inhibition. These findings indicate that spine size inversely correlates with the efficacy of local glutamate uptake and thereby likely determines the probability of synaptic crosstalk.

#### **INTRODUCTION**

The uptake of released neurotransmitters is an essential mechanism in synaptic transmission and prevents excitotoxic effects of the neurotransmitter glutamate. Its clearance is largely performed by astrocytic glutamate transporters (Danbolt, 2001; Rose et al., 2018). Therefore, the spatial proximity between astrocytic transporters and synaptic glutamate release sites determines how far glutamate can diffuse before it is taken up. For example, the physiological reduction of the coverage of neurons by astrocytes in the supraoptic nucleus during lactation is accompanied by a decreased uptake of synaptically released glutamate, which can increase the recruitment of presynaptic glutamate receptors (Oliet et al., 2001). Therefore, the degree of coverage of synapses by transporter-enriched astrocytic processes can represent an important parameter of synapse function.

In the rodent hippocampus, a key model for studying synaptic transmission and plasticity, electron microscopy studies of the CA1 *stratum radiatum* revealed that only ~40%–60% of synapses have astrocyte processes, which can be as thin as 100–200 nm, directly apposed (Ventura and Harris, 1999; Witcher et al., 2007). Numerous further studies have successfully established fundamental correlations between, for instance, the size

and morphological class of an individual spine, how much of its surface and boundary are directly contacted by astrocytic processes, and how much astrocytic process volume is nearby (Gavrilov et al., 2018; Genoud et al., 2006; Lushnikova et al., 2009; Medvedev et al., 2014; Patrushev et al., 2013; Ventura and Harris, 1999; Witcher et al., 2007, 2010). For example, we have previously demonstrated that the distance from postsynaptic densities to neighboring astrocyte processes differs between large mushroom spines and thin spines (Medvedev et al., 2014). However, the functional correlate of a difference in astrocytic coverage between postsynaptic spine types has remained largely unclear. Therefore, it also remains to be established which morphological aspects of astrocytic coverage are functionally relevant and for which biological processes.

Theory and numerical modeling predict that the geometry of synapses and adjacent astrocytes determine the spread and clearance of glutamate, activation of extrasynaptic receptors, and glutamate escape to neighboring synapses (Gavrilov et al., 2018; Medvedev et al., 2014; Rose et al., 2018; Zheng et al., 2008). Some of the predictions from these studies have more recently become testable by experimental means. We reasoned that if spine type and size determine the degree by which individual spines are covered by astroglial processes and thus by astrocytic glutamate transporters, then spine size would set the local



<sup>&</sup>lt;sup>2</sup>Department for Neurosurgery, University Hospital Bonn, Bonn, Germany

<sup>&</sup>lt;sup>3</sup>Research School of Chemistry, Australian National University, Canberra, Australia

<sup>&</sup>lt;sup>4</sup>Institute of Epileptology, Medical Faculty, University of Bonn, Bonn, Germany

<sup>&</sup>lt;sup>5</sup>Institute of Neurology, University College London, London, UK

<sup>&</sup>lt;sup>6</sup>German Centre for Neurodegenerative Diseases (DZNE), Bonn, Germany

<sup>&</sup>lt;sup>7</sup>Lead Contact

<sup>\*</sup>Correspondence: christian.henneberger@uni-bonn.de https://doi.org/10.1016/j.celrep.2020.108182





strength of glutamate uptake. As a consequence, spine size is expected to determine how well spines are also protected from a "spill-in" of glutamate from neighboring synapses and also how likely synaptically released glutamate escapes into perisynaptic space. In the present study, we explored these scenarios by taking advantage of super-resolution microscopy, glutamate imaging, and other techniques. We found that the local efficacy of glutamate uptake is low at large compared to small spines and correlates best with the amount of GLT-1 and astrocytic volume relative to the spine volume.

#### **RESULTS**

#### Superresolved Visualization of Perisynaptic Astroglial **Glutamate Transporters**

A quantitative assessment of the spatial relationship between glutamate transporters localized on perisynaptic astrocyte processes and synaptic spines requires high-resolution visualization of the spines and the leaf-like perisynaptic astrocyte processes, which can be as thin as 100-200 nm (Heller and Rusakov, 2015; Medvedev et al., 2014; Ventura and Harris, 1999). Here, we took advantage of expansion microscopy (ExM) (Asano et al., 2018; Chen et al., 2015; Chozinski et al., 2016), which provides the required resolution using well-characterized antibodies for standard confocal microscopy to label target proteins and structures. Indeed, ExM of astrocytes expressing cytosolic EGFP reveals the fine structural details of hippocampal astrocytes in the CA1 stratum radiatum at a drastically improved level (Figure 1A). Because of the improved resolution in all three dimensions, single focal sections display more clearly defined and much sparser astrocytic processes, more reminiscent of electron microscopy. Registration analysis revealed that the error introduced by either repetitive mounting for imaging and/or ExM is small and amounts to about 10% at the relevant sub-micrometer level (Figures S1A-S1C). We estimated the resolution achieved by ExM by using an immunolabeling of the synaptic protein Homer1 and could resolve objects as small as 40 nm in the x-y plane (Figures S1D-S1G), which provides an upper limit of the resolving power of ExM. Next, we combined ExM visualization of EGFP-expressing astrocytes with immunolabeling of the glutamate transporters GLT-1 and GLAST (Figures 1B and S2). In line with the notion that astroglial glutamate transporters mediate most of hippocampal glutamate uptake (Danbolt, 2001; Rose et al., 2018), GLT-1 labeling outlined EGFP-positive astrocyte processes. In addition, virtually all GLT-1-positive structures were EGFP positive (Figures 1B and S2A-S2D) and GLT-1 and GLAST colocalized (Figures S2E and S2F). We therefore used GLT-1 labeling to localize and characterize perisynaptic astrocyte processes carrying glutamate transporters around individual synaptic spines of CA1 pyramidal cells expressing yellow fluorescent protein (YFP) using ExM (Figure 1C).

The amount of GLT-1 immediately adjacent to individual spines on dendritic segments was quantified by determining the number of pixels positive for GLT-1 and YFP in spherical volumes of interest centered on spines (radius,  $r = 0.50 \mu m$ ; Figure 1D; also see STAR Methods). For each dendritic segment, the analyzed spines were then categorized as "small" or "large" if their volume (see STAR Methods) was below or above the median spine volume of that dendritic segment. We used the spine volume as a single measure of spine size throughout, instead of, for instance, threshold-based volume or surface renderings, because it can be readily obtained from ExM and two-photon excitation (2PE) microscopy data (see below), it is relatively insensitive to the optical resolution, and it does not require setting a threshold. We found that for volumes of interest with  $r = 0.50 \mu m$ , on average, the amount of GLT-1 was lower at small than at large spines on individual dendritic segments (Figure 1E). However, large spines have a higher surface area and a larger perimeter. A similar amount of GLT-1 could thus translate into a reduced density of glutamate uptake at the spine surface. We therefore also calculated the relative GLT-1 coverage by normalizing the number of pixels positive for GLT-1 and YFP to the spine size, i.e., spine volume. Indeed, GLT-1 was relatively less abundant at large spines (Figure 1F). We then asked if these findings change if the volume of interest is reduced by 40% ( $r = 0.42 \mu m$ ) and made qualitatively similar observations (Figures 1G and 1H). Next, we wondered if the dependence of GLT-1 coverage on spine volume would also hold for larger volumes of interest and set the radius of volumes of interest to 0.65  $\mu$ m, the average inter-synapse distance (Ventura and Harris, 1999). Here, we found that the raw abundance of pixels positive for GLT-1 and YFP, i.e., the amount of spine surface covered by GLT-1, was independent of spine volume. A likely explanation is that increasing the radius of analysis includes neighboring spines and dendritic shafts and thereby obscures spine size dependencies (Figures 1G and 1H).

Overall, these observations demonstrate that within a short distance the amount of GLT-1 is higher at large spines. However, when calculated relative to the spine volume, the GLT-1 coverage was smaller at big spines at all radii (Figure 1H). Similarly, we found a highly significant negative correlation between spine volume and the relative GLT-1 coverage at all analyzed radii (Figures S2G and S2H).

These results reveal that the size of an individual dendritic spine is a strong predictor of its coverage by astroglial GLT-1: the total surface of a large spine covered by GLT-1 is larger than that of a small spine. However, relative to their size, larger spines are generally less well covered by GLT-1. This raised two questions. First, does the efficacy of local glutamate uptake correlate with the absolute or relative abundance of GLT-1 at a spine? Second, does the volume of perisynaptic astrocyte processes display the same dependency on spine size?

#### **Spine Size Dependence of Local Distribution of Astrocytic Volume**

We have previously shown that the fluorescence of dye distributed in the astrocytic cytosol can be used as a measure of astrocytic process volume (Medvedev et al., 2014). Therefore, we used transgenic mice expressing EGFP under a GFAP promoter (Nolte et al., 2001) to visualize astrocyte processes using ExM. For the identification of excitatory synapses, we also labeled the presynaptic protein bassoon and the postsynaptic protein shank2, which is a component of the postsynaptic density

## **Article**



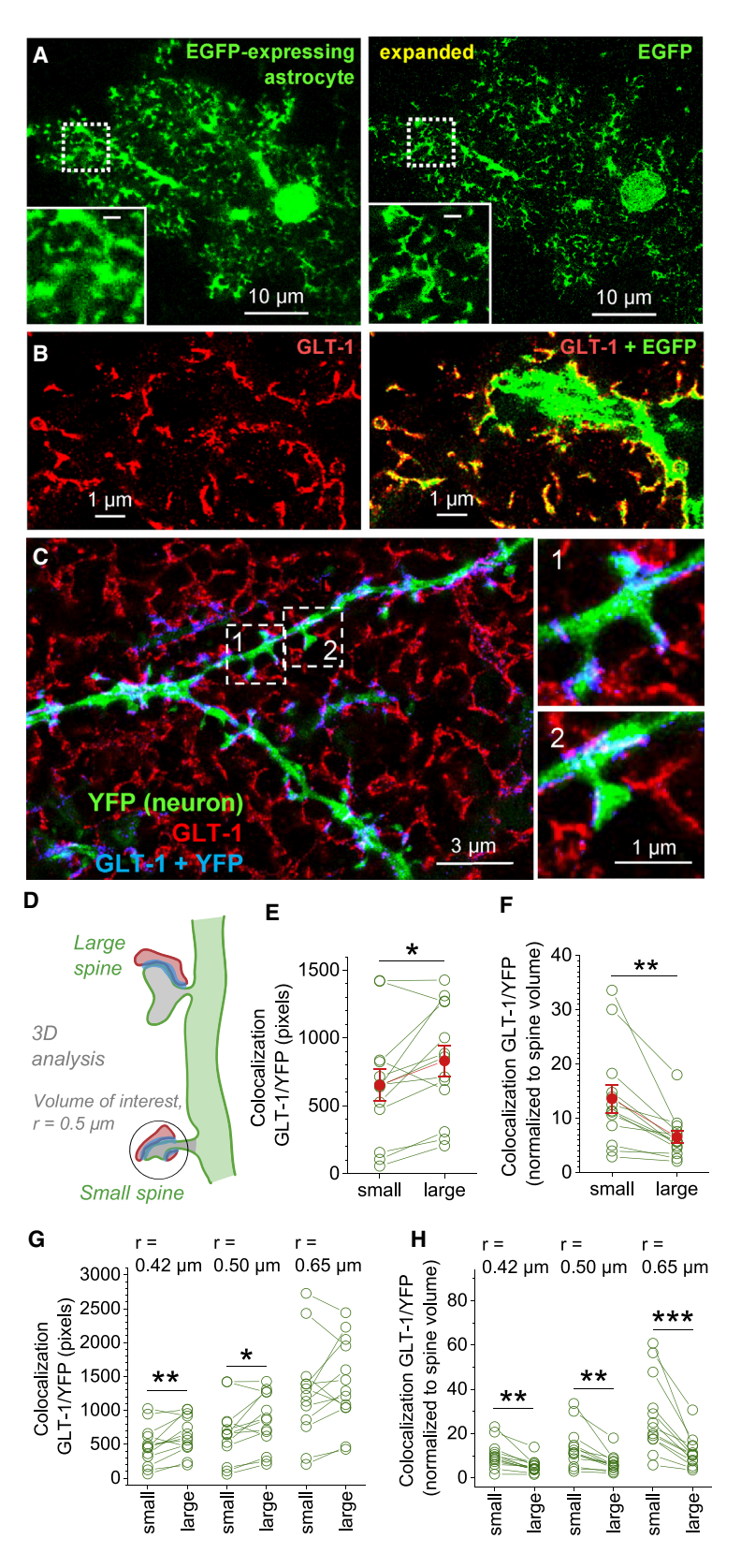


Figure 1. Expansion Microscopy (ExM) of Perisynaptic Astroglial Processes Reveals a Size-Dependent Coverage of Spines by the Astroglial Glutamate Transporter GLT-1 in Mouse CA1 Stratum Radiatum

(A) Example of a confocal image of the same astrocyte expressing EGFP before (left) and after (right panel) expansion (Chen et al., 2015; Chozinski et al., 2016). Scale bars correspond to pre-expansion dimensions (i.e., actual size/expansion factor for the right panel). See insets for higher magnification (scale bar, 1  $\mu$ m). Note the more clearly defined astrocyte branches in ExM and the disappearance of out-of-focus structures. See Figure S1 for a more detailed characterization of ExM. Note that only a subset of hippocampal astrocytes in these animals express EGFP (Nolte et al., 2001).

(B) ExM example of the glutamate transporter GLT-1 (left panel) and in combination with the visualization of an EGFP-expressing astrocyte (right panel). Note that virtually all GLT-1-positive structures colocalized with EGFP-positive astrocyte branches (yellow). Large branches are outlined by GLT-1 label. See Figure S2 for further examples of colocalization of glutamate transporters (GLT-1 and GLAST) and astrocyte branches.

(C) ExM of spines on a radial oblique dendrite of a CA1 pyramidal neuron (green, YFP) and the surrounding GLT-1 positive (red) astrocyte processes (left panel, see also Figure S2). Regions of immediate juxtaposition, i.e., appearing colocalized, are shown in blue. Numbered regions of interest (ROIs; dashed boxes): magnifications of sample ROIs (right panels).

(D) Illustration of the 3D analysis of GLT-1 coverage of individual spines. The total number of pixels positive for GLT-1 and YFP (blue, colocalization GLT-1/YFP in (E) was determined in spherical volumes of interest centered on the spine head ( $r = 0.50 \mu m$ ). Spines were categorized as "small" or "large" if their volume (see STAR Methods) was lower or higher, respectively, than the median spine volume on the analyzed dendritic branch. In total, 347 spines from 13 dendritic segments obtained from 4 separate experiments were analyzed.

(E) The total number of pixels positive for GLT-1 and YFP was significantly lower at small spines than at large spines (r = 0.50  $\mu$ m). Connected circles represent the average number of pixels at small and large spines of a single dendrite (paired data). Red data points represent averages and SEM across all analyzed dendrites. Paired Student's t test on 13 individual dendrites, p = 0.0220; n = 13 dendrites.

(F) Relative to the individual spine volume, smaller spines are more strongly covered by GLT-1 (r = 0.50  $\mu$ m). For all spines across all experiments, the GLT-1/YFP colocalization in pixels was normalized to the spine volume to obtain the relative abundance of GLT-1 at small and large spines. Data presentation as in (E). Relative GLT-1 coverage is higher at small spines than at large spines (paired Student's t test, p = 0.00223; n = 13

(G) Comparison of GLT-1/YFP colocalization between small and large spines with differently sized volumes of interest  $(r = 0.42 \mu m, 0.50 \mu m and 0.65 \mu m from left to right)$ . Data for r = 0.50  $\mu m$  is replotted from (E). Paired Student's t tests, p = 0.00942, 0.0220, and 0.237 from left to right; n = 13 dendrites. (H) Analysis of colocalization relative to spine volume with differently sized volumes of interest, as in (G). Paired Student's t tests, p = 0.00108, 0.00223, and 0.000359 from left to right; n = 13 dendrites.



(PSD) of glutamatergic synapses (Sheng and Hoogenraad, 2007). This ExM triple labeling allowed us to localize glutamatergic synaptic contacts within the territory of single astrocytes (Figure 2A). For 3D analysis, we pseudo-randomly chose volumes of interest containing single putative synaptic contacts (see STAR Methods) with directly apposed pre- and postsynaptic label (without inspection of the local EGFP fluorescence to avoid a selection bias). We then analyzed the fluorescence intensity of EGFP, i.e., the astroglial volume distribution in spherical shells with increasing diameter centered on the PSD (Figure 2A, bottom right panel; STAR Methods). The center of the PSD was chosen because we were interested in how abundant astrocyte processes are close to the postsynaptic receptors. In total, we analyzed 151 volumes of interest covered by 8 different astrocytes from 3 independent experiments. As above, we categorized the PSDs as small or large depending on whether their volume (see STAR Methods ) was lower or higher, respectively, than the median PSD volume for the studied astrocyte territory. We found that the sum of EGFP fluorescence within shells continuously increased with distance, whereas the density within the spherical shells reached a plateau at about 300-400 nm, which is similar to results of a previous study using electron microscopy (Patrushev et al., 2013). No difference between the profiles at small and large PSDs was observed (Figures 2B and 2C). As expected from this observation, the cumulative EGFP fluorescence within a radius of 1 µm was not significantly different when we compared small and large PSDs within the territory of single astrocytes (Figure 2D). Therefore, the absolute volume of perisynaptic astroglial processes in the immediate vicinity of a glutamatergic synapse does not depend on the size of its PSD and, because PSD size and spine volume are strongly correlated (Harris and Stevens, 1989; Lushnikova et al., 2009), not on spine size. Because absolute GLT-1 surface coverage displayed a spine size dependence at a short distance, this finding suggests that the surface-to-volume ratio of astrocytic processes differs between small and large spines.

Larger spines could also have bigger presynaptic terminals with larger active zones and a higher release probability (Holderith et al., 2012; Murthy et al., 2001; Schikorski and Stevens, 1997). This could lead to stronger astrocytic sodium accumulation during uptake and thereby to an impairment of glutamate uptake, for review (Rose et al., 2018), if the increase of release probability at large spines is not matched by an increase of perisynaptic astrocyte volume. To quantify the relative abundance of perisynaptic astrocyte volume, we normalized the cumulative EGFP fluorescence to the PSD volume. We found that this relative measure of astrocyte volume around a PSD is significantly lower at large PSDs (Figure 2E). Although we have analyzed EGFP fluorescence in Figures 2E and 2F for a radius of 1 μm, which may include undetected neighboring spines, this finding will apply to shorter distances because the profiles in Figures 2B and 2C are virtually identical (also see legend).

This again raised the question if the relative scarceness of astrocyte processes leads to less effective glutamate uptake at glutamatergic synapses with large postsynaptic spines or PSDs. To address this question, we next performed experiments that directly assess the efficacy of glutamate clearance at individual spines.

#### The Efficacy of Local Glutamate Clearance is Lower at **Large Spines**

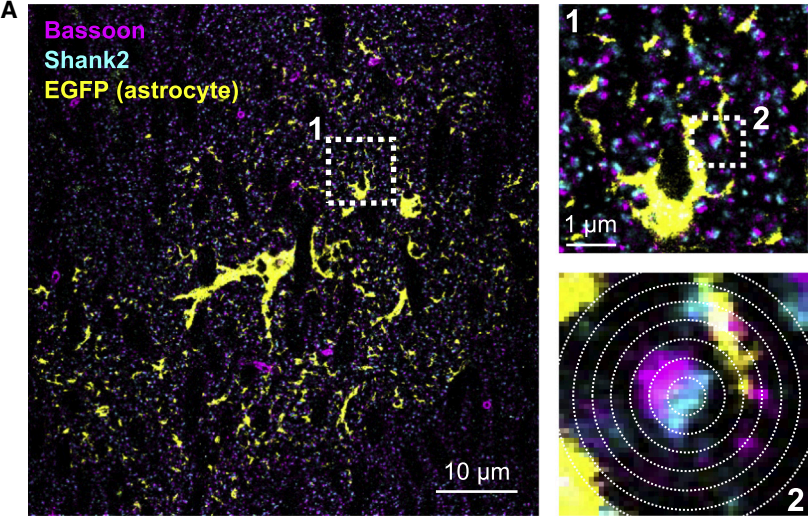
To investigate the functional role of the dependency between the amount of perisynaptic astroglia and the spine/PSD size, we visualized glutamate transients at individual spines triggered by synaptic glutamate release. This was achieved by viral expression of the optical glutamate sensor iGluSnFR (Marvin et al., 2013) on the surface of astrocytes and observation of its fluorescence using 2PE microscopy in the CA1 stratum radiatum of acute hippocampal slices (Figure 3). Individual spines of CA1 pyramidal cells were imaged simultaneously after loading a single cell with Alexa Fluor 594 (by a whole-cell patch pipette, pipette withdrawal after 10 min). Extracellular glutamate transients were induced by electrical stimulation of CA3-CA1 axons with brief bursts (10 pulses at 100 Hz) with glutamate receptors blocked. Responses were readily detectable at sets of simultaneously monitored individual spines (Figures 3A-3C). Using this experimental paradigm, we then quantified the local strength of glutamate uptake by the sensitivity of the recorded glutamate transients to pharmacological partial blockade of glutamate transporters using 200 nM TFB-TBOA (bath application). Although TFB-TBOA does not inhibit a specific transporter at this concentration and bath application is not cell-type specific, we used this approach because the astroglial transporters GLT-1 and GLAST far outnumber other glutamate transporters in this brain region and are mostly localized on astrocytes (Holmseth et al., 2012; also see Figure S2).

We first analyzed the global effect of TBOA and found that the area under the curve (AUC,  $\Delta F/F_0 \times ms$ ), which we chose in order to capture changes of amplitude and decay, increased after application of TBOA but not in control experiments (Figure S3). To investigate the effect of TBOA on the level of single spines, we then calculated the difference between the AUC during baseline and after TBOA application (TBOA effect,  $\Delta$ AUC = AUC<sub>TBOA</sub> AUC<sub>baseline</sub>) at individual spines (for example, see Figure 3D). Again, spine volumes were analyzed and expressed relative to the median volume of 10 spines on the same dendritic segment. The overall magnitude of the TBOA effect varied between recordings (three examples in Figure 3E), but a negative correlation between the TBOA effect and spine volume appeared to be a consistent finding. A potential explanation is that TBOA could increase the resting glutamate levels, thereby increasing F<sub>0</sub> and thus downscaling  $\mbox{AUC}_{\mbox{\scriptsize TBOA}}$  across spines. To analyze the pooled data, we therefore aligned data by subtracting the mean TBOA effect at a dendrite from each data point of that dendrite (see filled orange circles representing a single experiment in Figures 3D-3F). Performing this analysis across 65 spines (from 12 dendrites in independent experiments), we revealed a statistically significant negative correlation between the glutamate transient sensitivity to TBOA and the spine volume (Figure 3F).

Our findings indicate that the perisynaptic concentration of synaptically released glutamate is more strongly affected by transporter blockade at small than at large postsynaptic spines. In other words, glutamate transients at small spines are more tightly controlled by glutamate transporters than at large spines. Comparing these findings to the morphological data obtained by ExM, this shows that the local uptake efficacy changes in parallel

## **Article**





analysis of perisynaptic astroglial EGFP in spherical shells

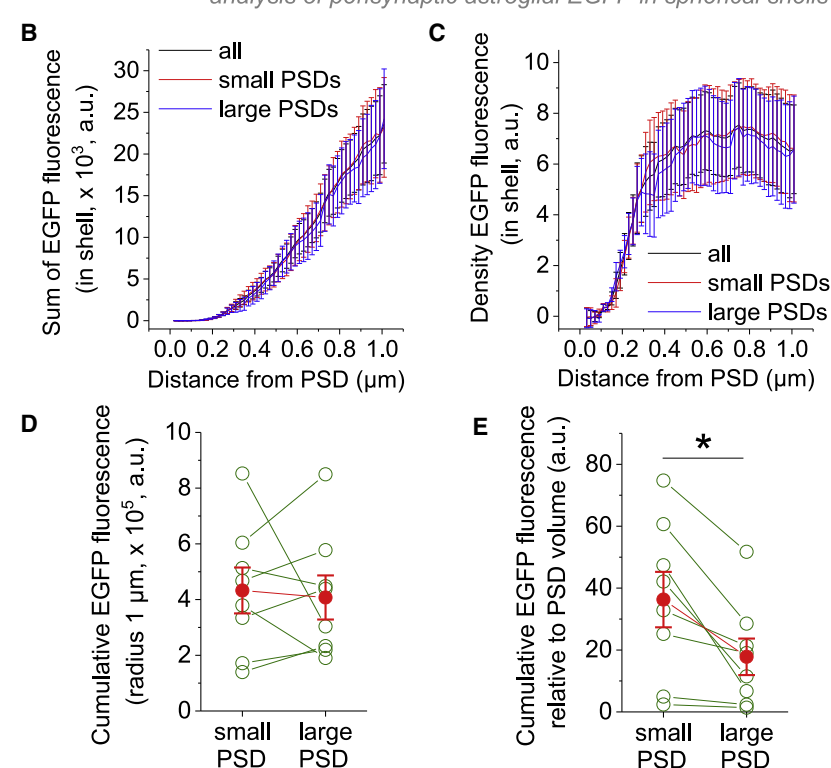


Figure 2. Dependence of the Volume of Perisynaptic Astrocytic Processes on the Size of the Postsvnaptic Density (PSD)

(A) ExM of EGFP-expressing astrocytes and pre- and postsynaptic sites (example of a single focal plane). Left panel: low-magnification examples of a triple-label ExM experiment (astrocyte: cytosolic EGFP, yellow; presynaptic label: bassoon, magenta; PSD label: shank2, cyan). The empty elongated regions most likely represent cross sections of pyramidal cell dendrites. Top right panel: enlarged section from boxed region (white, 1) in left panel. Bottom right panel: further magnified view from top right panel (white box, 2). Size, 1.25  $\times$  1.25  $\mu$ m<sup>2</sup>. Analysis was performed in 3D by quantifying astroglial EGFP fluorescence in spherical shells centered on the shank2 label (3 independent experiments, 8 astrocytes, 151 putative synapses). See Results and STAR Methods for further details.

(B) The summed up EGFP fluorescence intensities in spherical shells with increasing radius were calculated (all spines: black). For each analyzed astrocyte, PSDs were categorized as small or large if their volume was below or above the median PSD volume within that astrocyte, respectively (see STAR Methods). The EGFP fluorescence profiles were averaged and displayed for both categories (mean  $\pm$  SEM, in all panels). The profiles for small and large PSDs were not different (repeatedmeasures two-way ANOVA, p < 0.0001 for distance, p = 0.908 for PSD size).

(C) The volume density of EGFP fluorescence intensity was calculated similarly to (B). Again, the EGFP density distribution was not different between small and large PSDs (repeated-measures two-way ANOVA, p < 0.0001 for distance, p = 0.916 for PSD size).

(D) The cumulative intensity of astroglial EGFP fluorescence within a radius of 1  $\mu m$  around the PSD was calculated for small and large PSDs covered by individual astrocytes and compared. No statistically significant difference was found (paired Student's t test, p = 0.783, n = 8 astrocytes).

(E) The cumulative intensity of astroglial EGFP fluorescence was normalized to the PSD size and then compared between small and large PSDs for each astrocyte as in (D). Relative to their size, large PSDs were surrounded by less astrocyte volume (paired Student's t test, p = 0.0106, n = 8 astrocytes).

with the relative and not the absolute amount of local GLT-1 and astroglial volume at spines. These observations also imply that the stronger local glutamate uptake shields small spines particularly well from glutamate released nearby, for instance at neighboring synapses.

#### **Invasion of Glutamate Depends on Spine Size**

We directly tested this hypothesis by combing 2PE fluorescence imaging and glutamate uncaging with whole-cell patch clamp recordings (Matsuzaki et al., 2001; Smith et al., 2003; Sun et al., 2016) of excitatory postsynaptic currents (EPSCs) mediated by N-methyl-D-aspartate receptors (NMDARs). NMDAR EPSCs were chosen in these experiments because of their relatively high affinity to glutamate. Dendrites and spines of individual CA1 pyramidal cells were visualized using 2PE fluorescence microscopy, and glutamate was first uncaged directly at the head of a pseudo-randomly chosen spine (Figure 4A, #1). The NMDAR-mediated component of the uncaging-evoked EPSCs (uEPSCs) was isolated pharmacologically and by recording at a holding potential of +40 mV. The recorded uEPSCs were



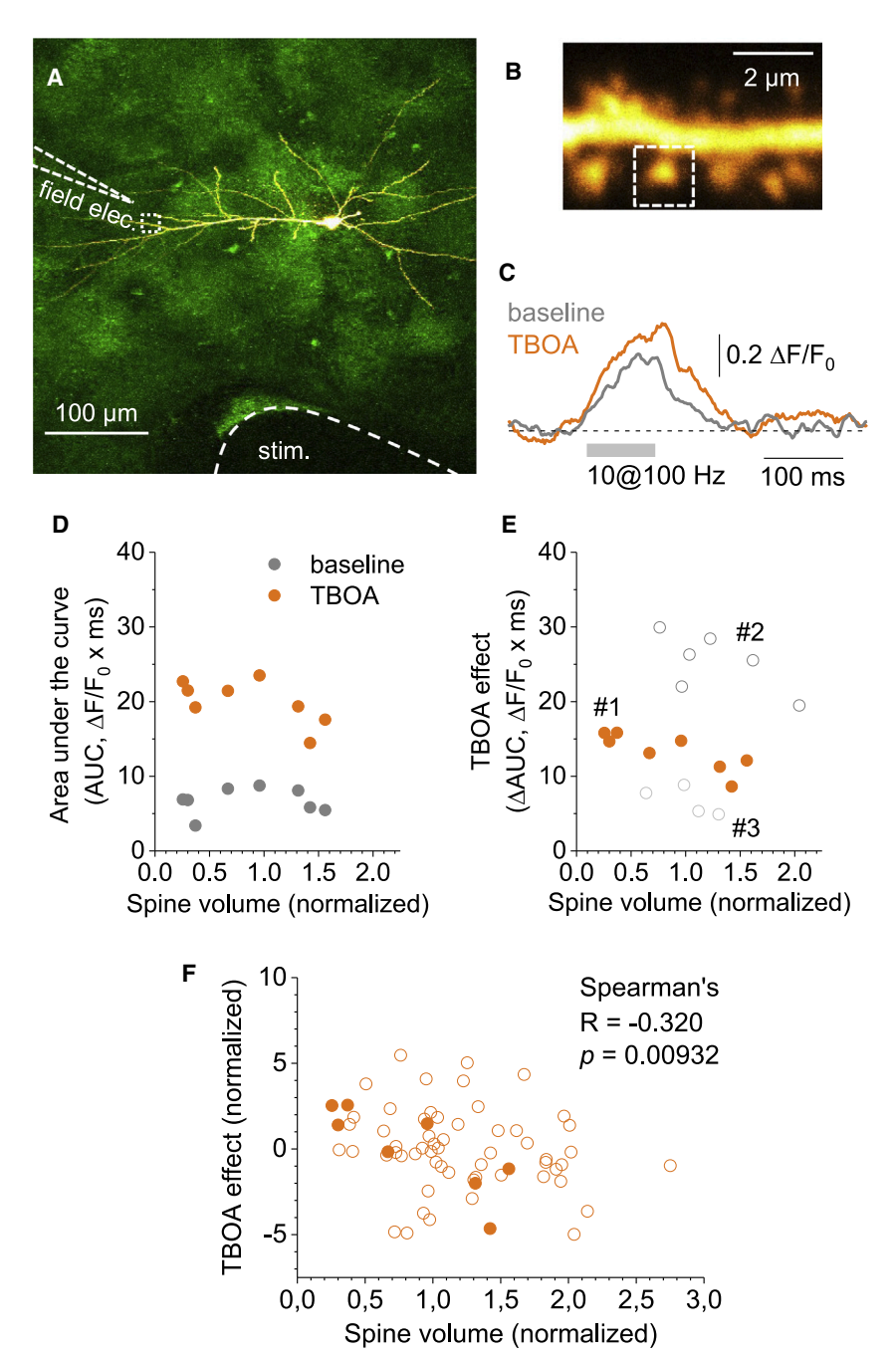


Figure 3. Perisynaptic Glutamate Transients Are More Tightly Controlled by Glutamate Transporters at Small Postsynaptic Spines **Than Larger Neighbors** 

(A) Astrocytic expression of the glutamate sensor iGluSnFR (green; Marvin et al., 2013) visualized in acute hippocampal slices by two-photon excitation fluorescence microscopy. Note that the majority of astrocytes express iGluSnFR. A CA1 pyramidal neuron (yellow) was filled with Alexa Fluor 594 to localize and investigate its spines (dashed box, region of interest [ROI], see B). A field electrode (field elec.) was placed near its dendritic arbor in the stratum radiatum and CA3-CA1 axons, i.e., Schaffer collaterals were electrically stimulated (stim.; field responses not shown). Experiments were done in the presence of 50 µM D-APV, 10 µM NBQX, and 100 μM LY341495.

- (B) Sample dendritic segment with spines of different sizes (magnified from A; only Alexa Fluor 594 shown) with a ROI positioned on an individual spine.
- (C) iGluSnFR fluorescence transients around dendritic spines (B) in response to axonal stimulation (50 sweeps of 10 pulses at 100 Hz every 20 s) were recorded (baseline, dark gray trace) and the effect of the glutamate transporter inhibitor TFB-TBOA (200 nM) was analyzed (orange).
- (D) The area under the curve (AUC,  $\Delta F/F_0 \times ms$ ) of iGluSnFR fluorescence transients during a baseline recording and after TBOA application were analyzed. Example of a simultaneous recording from eight dendritic spines. For each spine, the volume was measured and normalized to the median spine volume on that dendritic segment. Vertically aligned baseline/TBOA data points represent the same spine during baseline and TBOA.
- (E) The TBOA effect was quantified by calculating the AUC difference between TBOA and baseline. #1 corresponds to (D). #2 and #3 represent two other examples.
- (F) Summary data from 65 spines (open circles, 12 independent experiments, data obtained from spines in B-D as solid circles). For each set of recorded spines, the average TBOA effect (ΔAUC) was subtracted before pooling all data (see Results). The TBOA effect displayed a negative correlation with the normalized spine volume, suggesting a higher uptake capacity at small spines (Spearman's rank correlation, p = 0.00932, R = -0.320).

mediated almost exclusively by NMDARs because addition of the NMDAR inhibitor APV (50  $\mu$ M) to the extracellular solution reduced the uEPSC amplitude by >95% (control: 14.7  $\pm$ 4.60 pA, n = 5 cells [156 spines in total], APV: 0.489  $\pm$ 0.105 pA, n = 5 cells [264 spines in total], not illustrated).

Next, we recorded NMDAR uEPSCs at two different distances from the spine, immediately adjacent and at a distance of 500 nm (Figure 4A, #1 and #2). First, we analyzed if the amplitude or the decay time constant of NMDAR-mediated uEPSCs evoked by uncaging immediately at the spine (#1) correlated with spine

size, which was not the case (Figure S4). Second, if the NMDARs mediating the uEPSCs are shielded well from invading glutamate, then moving the site of glutamate uncaging away from the spine should reduce the uEPSC amplitude. The increased average distance that uncaged glutamate needs to travel to the recorded NMDARs could, for instance, increase the probability of glutamate binding to glutamate transporters before reaching recorded NMDARs. This attenuation of the NMDARmediated response was calculated as I<sub>Glu. 0 nm</sub>/I<sub>Glu. 500 nm</sub> for recordings at 21 spines (Figures 4B and 4C for example). Given the





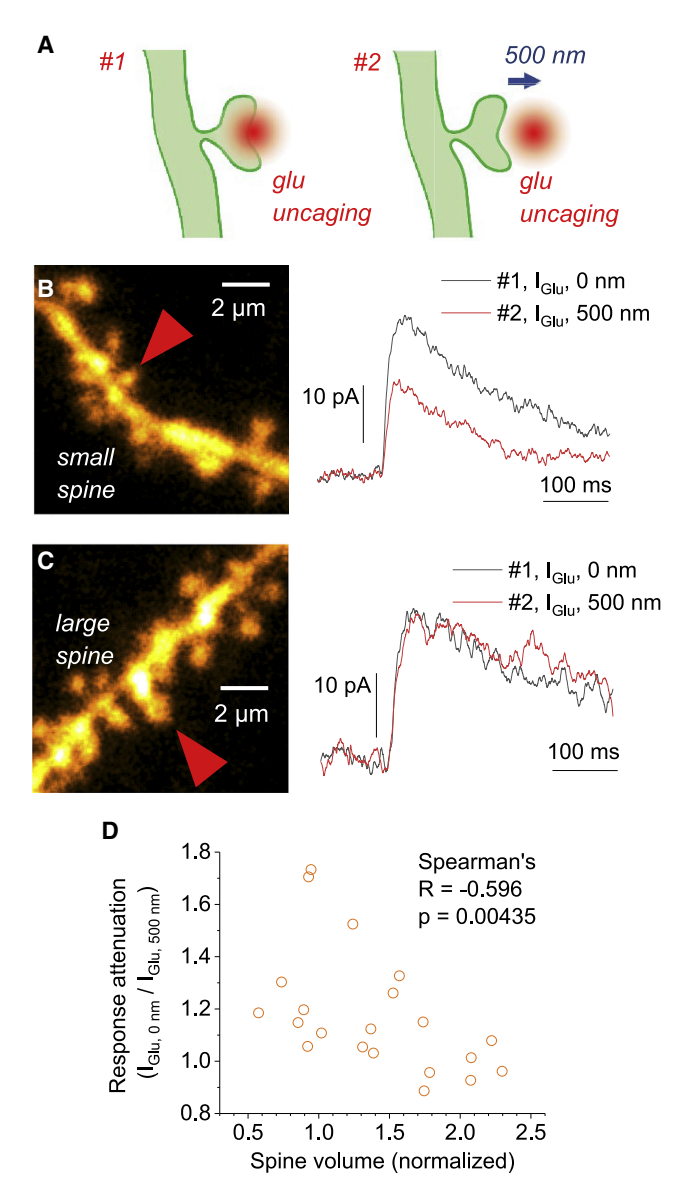


Figure 4. NMDA Receptors (NMDARs) at Small Spines Are More Strongly Protected from Invading Glutamate Than Larger Spines

(A) Schematic illustration of the experimental approach. NMDAR-mediated excitatory postsynaptic currents (EPSCs) were recorded from CA1 pyramidal cells and evoked by two-photon uncaging of glutamate (uEPSC). uEPSC recordings at two different distances from the spine head were obtained by sequential uncaging at 0 nm (#1) and 500 nm (#2). Three of such recordings were recorded for a given spine and averaged for analysis. The uncaging response recorded at 500 nm (#2) is expected to be smaller if, for instance, NMDARs are efficiently shielded by local glutamate transporters.

- (B) Example of an uncaging experiment at a relatively small spine. Left panel: dendritic segment; red arrow indicates investigated spine. Right panel: NMDAR-mediated EPSCs at distance #1 (black trace) and #2 (red trace). Note the amplitude reduction after moving the uncaging spot 500 nm away from
- (C) As in (B) for a larger spine from another cell. Note the absence of an amplitude reduction in this example.
- (D) For each spine, the uEPSC attenuation (I $_{\rm Glu,\ 0\ nm}/$  I $_{\rm Glu,\ 500\ nm}$ ) and the spine volume relative to the median spine volume of the corresponding dendritic segment were calculated. Overall, a statistically significant negative correla-

high relative amount of GLT-1 (ExM) and the high efficacy of glutamate uptake (iGluSnFR imaging) at small spines, we expected better shielding of NMDARs and thus a higher attenuation of the uEPSC amplitude at small dendritic spines. This was tested by correlating the spine volume (normalized to the median spine volume of the corresponding dendrite) to the attenuation of the NMDAR-mediated EPSCs (average attenuation of  $1.18 \pm 0.051$ , n = 21). Indeed, a statistically significant negative correlation was observed (Figure 4D). On its own, this finding may also be explained by different properties of the extracellular space (ECS), into which glutamate is uncaged, and NMDAR properties or distributions at spines of different sizes. However, consistent differences of NMDAR density and subunit composition between large and small spines would also be expected to affect the absolute uEPSC amplitudes and decay time constants (Cull-Candy and Leszkiewicz, 2004). Because neither was observed (Figures S4B and S4C), the stronger attenuation of uEPSCs at small spines likely reflects the spine size dependence of the local efficacy of glutamate uptake and of the relative amount of local GLT-1 and astrocyte process volume, as described above.

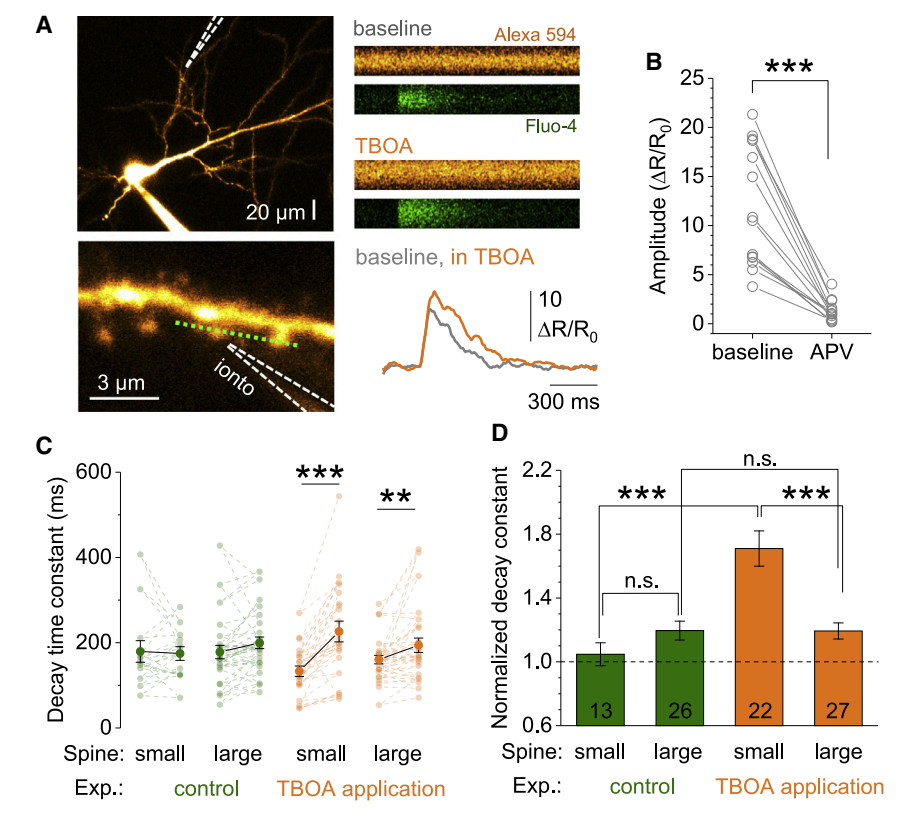
## Control of NMDAR-Mediated Ca<sup>2+</sup> Entry by Glutamate **Uptake Depends on Spine Size**

In the next set of experiments, we further explored how the local control of NMDAR function by glutamate uptake depends on spine size. Because of the importance of NMDAR-mediated Ca<sup>2+</sup> entry for synaptic plasticity, we focused on NMDAR-mediated Ca<sup>2+</sup> transients. In these experiments, release of glutamate into the neuropil was emulated by iontophoretic application of glutamate while monitoring Ca<sup>2+</sup> entry in nearby spines by using established techniques (Minge et al., 2017). CA1 pyramidal cells were filled with Alexa Fluor 594 and the Ca2+ indicator Fluo-4 and held in the whole-cell voltage clamp configuration (Figure 5A). We then identified a set of spines on a dendritic segment of that cell, placed an iontophoresis pipette nearby, and used Ca<sup>2+</sup> influx through the high-affinity NMDARs as a detector of glutamate invasion of the synaptic environment (holding voltage at -20 mV). The ratio (R) of the fluorescence intensities of the Ca<sup>2+</sup>-indicator Fluo-4 and Alexa Fluor 594 was used as a measure of intracellular Ca2+. Glutamate iontophoresis induced clearly defined Ca<sup>2+</sup> responses in spines, which were largely inhibited by the NMDAR antagonist APV (Figures 5A and 5B).

The local efficacy of glutamate uptake in shielding synapses from invading glutamate was then tested by pharmacological inhibition of glutamate uptake (200 nM TFB-TBOA) and compared to control recordings, in which no TBOA was added. In both sets of experiments, a baseline recording was obtained first and then a second control recording (green data pairs and bars) or a recording in TBOA (orange data pairs and bars) was acquired. Spine volumes were determined as before and normalized to

tion was observed (Spearman's rank correlation, R = -0.596, p = 0.00435; n = 21 spines, from 21 different dendrites, 7 pyramidal cells, 5 animals). Note that there was a tendency to pick spines for uncaging experiments that turned out to be relatively large during analysis (normalized volume > 1.0 for 15 out of 21 spines). The strength of the true correlation could, therefore, be underestimated.





5. Glutamate Uptake **Controls** NMDAR-Mediated Ca2+ Entry More Effectively at Small Spines Than at Large Ones

(A) Example of a CA1 pyramidal neuron patched and filled with Alexa Fluor 594 (orange) and the Ca2+ indicator Fluo-4 (top left panel). Glutamate application by iontophoresis near spines (bottom left panel, dashed lines; average distance to closest spine, 3.9  $\pm$  0.2  $\mu$ m; n = 12) was combined with postsynaptic depolarization in order to use NMDAR-dependent Ca2+ entry as an indicator of glutamate invasion. Simultaneous line scans (bottom left panel, dotted green line) of Fluo-4 and Alexa Fluor 594 fluorescence across multiple spines (sample line scans, top right panels; total duration, 1,350 ms). The ratio (R) of Ca2+-indicator (Fluo-4) and Alexa Fluor 594 fluorescence intensities was used as a measure of intracellular Ca2+ (STAR Methods). Note the prominent Ca2+ entry representing glutamate entering extracellular space around spines and the effect of inhibiting glutamate transporters with TFB-TBOA (200 nM). All experiments were performed in the presence of 1 µM TTX,  $20~\mu\text{M}$  nifedipine,  $10~\mu\text{M}$  NBQX,  $10~\mu\text{M}$  MPEP, and 50 μM LY341495.

(B) Ca<sup>2+</sup> transients were highly sensitive to NMDAR inhibition by APV (50 μM). Amplitudes were quantified in this experiment as the ratio of the peak  $\Delta R$ and R<sub>0</sub>, the pretransient baseline. Residual amplitudes in APV were 12.4% ± 1.86% of the pre-APV values (p < 0.0001, Student's paired t test; n = 12). (C) Spine Ca2+ transients were recorded a first time to obtain a baseline measurement. In control recordings (green data points), a second recording

was performed 8 min later under the same conditions. In experiments probing the strength of glutamate uptake (orange data points), TBOA was applied by the extracellular bath solution and a second recording was obtained. Spines were categorized as small or large if their volume (STAR Methods) was below or above, respectively, the median spine volume of the corresponding dendritic segment. The effects on the decay of Ca<sup>2+</sup> transients were analyzed (see Figure S5 for further details). Each pair of data points connected by a dashed line represents a single spine during baseline and after a control period or TBOA application. Averages with SEM connected by solid lines. Paired Student's t tests (p = 0.796, p = 0.0501, p < 0.0001, and p = 0.00129 from left to right).

(D) The relative change of the decay time constant in control and TBOA experiments was calculated by normalizing the decay time constant of the second measurement to that of the baseline period for each spine. Two-way ANOVA analysis identified significant effects of spine size (small versus large, p = 0.0216), treatment (control versus TBOA, p < 0.0001), and a significant interaction between both (p < 0.0001). Post hoc analysis using the Tukey test revealed that the effect of TBOA was significantly higher in small than in large spines (p < 0.0001), whereas spine volume played no statistically relevant role in control recordings (p = 0.608, n.s.). Similarly, a statistically significant difference between control and TBOA recordings was observed for small spines (p < 0.0001) but not for large spines (p = 1.00).

Control experiments: n = 13 small and 26 large spines, recorded from 11 dendritic segments of 11 cells; TBOA experiments: n = 22 small and 27 large spines, recorded from 15 dendritic segments of 15 cells). See Figure S5 for further analyses. Averages with SEM.

the median spine volume on the dendritic segment. Statistical analyses of the recordings are shown in Figures 5C, 5D, and S5. It is noteworthy that similar to glutamate uncaging experiments, we observed no correlation between spine volume and the properties of Ca2+ transients obtained during baseline recordings (Figures S5A-S5C). After TBOA application, we detected increases in the resting Ca<sup>2+</sup> levels (Figure S5D), which is likely the consequence of the previously documented TBOAinduced increase of tonic NMDAR currents (Cavelier and Attwell, 2005; Le Meur et al., 2007), and an unspecific rundown of Ca2+ transient amplitudes in most experimental conditions (Figure S5E), which is probably due to strong Ca<sup>2+</sup> influx after repetitive holding potential increases and glutamate applications at relatively distal dendrites (Rosenmund and Westbrook, 1993). In contrast, the decay time constant was stable in control recordings, and changes of the decay time constant of NMDAR-mediated currents have previously been shown to follow changes of glutamate uptake (Armbruster et al., 2016; Romanos et al., 2019). The decay time constant was therefore used as a readout of a spine-size-specific effect of TBOA (Figures 5C and 5D).

We found that TBOA selectively increased the decay time constant of Ca2+ transients at small but not at large spines (Figure 5D). This finding is further supported by a statistically highly significant negative correlation between the normalized spine volume and the effect of TBOA on the Ca2+ signal decay time constant (Spearman's rank correlation, R = -0.589, p < 0.0001, n = 49 spines), which was not observed in control experiments (R = 0.011, p = 0.947, n = 39 spines). Importantly, experimentally measured changes of the decay time constant were statistically independent of unspecific rundown (Spearman's rank correlation, R = -0.0268, p = 0.856, n = 88 spines spines) and changes of Ca<sup>2+</sup> resting levels (Spearman's rank correlation,

### **Article**



R = 0.0939, p = 0.521, n = 88 spines). Together, these observations indicate that the dwell time of iontophoretically applied glutamate in the perisynaptic environment is more tightly controlled by glutamate uptake at small spines than at large spines. They also provide a third line of evidence for a higher local glutamate uptake efficacy at small than at large spines. Probing glutamate handling at single spines of various sizes thus revealed an inverse relationship between postsynaptic spine size and the local efficacy of glutamate uptake, which matches the negative correlation between the relative amount of local GLT-1 and astrocytic process volume and spine size.

#### **DISCUSSION**

A variable coverage of glutamatergic synaptic terminals by astrocytic processes and a large percentage of synapses without immediately apposed astrocytic processes are consistent findings in the literature (Gavrilov et al., 2018; Korogod et al., 2015; Lushnikova et al., 2009; Medvedev et al., 2014; Patrushev et al., 2013; Ventura and Harris, 1999; Witcher et al., 2007, 2010). This raised unanswered questions about the functional relevance of differential astrocytic synaptic coverage, for instance for glutamate uptake, and the mechanisms that determine it. Here, we took advantage of more recently developed techniques like ExM to visualize glutamate transporters (GLT-1) and astrocyte volume in the vicinity of synapses and spines (Chen et al., 2015; Chozinski et al., 2016). We then correlated our findings with optical probing of glutamate dynamics with single-spine resolution to establish the functional correlate of differential astrocytic coverage of spines with different sizes.

Investigating the abundance of GLT-1 at the spine surface by using ExM, we found that the total amount of GLT-1 immediately at the spine surface is higher at big spines than at small ones when analyzed close to the spine. Because the strong GLT-1 label in ExM reliably outlined the astrocyte cytosol (Figures 1 and S2), this relationship is likely to also apply to the absolute amount of astrocyte membrane in direct apposition with the spine, which would be in line with a previous report using electron microscopy (Lushnikova et al., 2009). A similar dependency between spine size and the volume of perisynaptic astrocyte processes was not found, which is overall in line with previous studies using electron microscopy (Gavrilov et al., 2018; Patrushev et al., 2013). In addition to the absolute GLT-1/spine colocalization and perisynaptic astroglial volume, we also determined each parameter relative to the spine size for two reasons. First, the amount of GLT-1 relative to the spine size, i.e., the GLT-1 density could determine how well the postsynaptic receptors are covered and protected by glutamate uptake and how likely glutamate can escape from the active synapse. Second, the number of docked vesicles, the active zone size, the release probability, and the size of spines and PSDs are positively correlated (Bartol et al., 2015; Harris and Stevens, 1989; Holderith et al., 2012; Murthy et al., 2001; Schikorski and Stevens, 1997), and glutamate uptake leads to astrocytic sodium entry (Danbolt, 2001; Rose et al., 2018). Therefore, the relative abundance of perisynaptic astrocyte cytosol could determine how easily sodium accumulates in astrocytes and whether that leads to a reduction of the sodium driving force of glutamate uptake. We consistently found that both the amount of GLT-1 at the spine surface and astrocytic process volume relative to the spine size were lower at large than at small spines.

It is important to note that in these experiments and other work using similar tissue fixation protocols, for instance for electron microscopy, ECS is often collapsed. The ECS normally accounts for ~20% of living tissue volume in CA1 stratum radiatum (Syková and Nicholson, 2008) and amounts to about double the fraction of tissue volume taken up by astrocytes (Korogod et al., 2015; Medvedev et al., 2014). Chemical fixation can thereby lead to morphological alterations of perisynaptic astrocyte processes and more increased direct apposition of neuronal and astrocytic membranes (Korogod et al., 2015). Indeed, a recent study using STED superresolution microscopy in live organotypic slices discovered new morphological features of astrocytes, such as nodes, shafts, and loops (Arizono et al., 2020). Given the many possible measures of astrocytic coverage of spines and the potential drawbacks of preparations and methods, it is important to establish a functional correlate of astrocytic coverage of synapses. We therefore probed the local efficacy of glutamate uptake and extracellular glutamate spread.

Using glutamate uncaging, we could demonstrate that small spines are better shielded from the invasion of glutamate than larger spines. This individual finding could also be explained by a different ECS configuration (e.g., tortuosity) at small and large spines. New optical methods that visualize the ECS on the nanometer scale in living tissue using STED microscopy (Tønnesen et al., 2018) or imaging of carbon nanotubes (Godin et al., 2017) and mapping the proximity of neuronal and astrocytic surfaces using FRET probes (Octeau et al., 2018) could be useful for testing if the ECS indeed displays spine-size-dependent configurations. Such information would also be useful for modeling glutamate diffusion at spines with different sizes. To estimate the local efficacy of glutamate uptake more directly, we measured the effect of pharmacological glutamate uptake inhibition on glutamate transients evoked by synaptic stimulation and NMDAR-mediated Ca<sup>2+</sup> entry in response to iontophoretic glutamate application at single spines of various sizes. We consistently found that uptake inhibition had a larger effect at small spines, which indicates that glutamate uptake is more effective at these spines. This result can directly explain why these spines were better shielded in uncaging experiments. Under baseline/ control conditions, NMDAR-mediated currents or Ca2+ entry did not show a clear spine size dependence (Figures S4 and S5A-S5C), which is likely due to the variations of the uncaging spot position relative to the PSD, amount of uncaged glutamate, and of the placement of the iontophoretic pipette between experiments. Instead, the spine size dependence of the uptake efficiency was robustly unmasked by inhibition of glutamate uptake and moving the glutamate uncaging spot. It is also noteworthy that the size of this effect is not expected to be quantitatively identical between experimental approaches because iGluSnFR fluorescence, NMDAR currents, and especially Ca<sup>2+</sup> transients, which could also be affected by endogenous buffers and extrusion mechanisms, are non-linear readouts of the extracellular glutamate concentration.

On a qualitative level, all functional experiments pointed toward a higher efficacy of glutamate uptake at small spines.



Because the spine volume of CA1 pyramidal cell dendrites is tightly correlated with the PSD size and the number of presynaptic vesicles (Bartol et al., 2015; Harris and Stevens, 1989; Murthy et al., 2001), our observations imply that, in general, astrocytic glutamate uptake at synapses with a small vesicle pool, small PSD, and low spine volume is particularly effective in constraining extracellular glutamate diffusion. The magnitude of this effect is likely to be underestimated in the present experiments using diffraction-limited 2PE microscopy (Figures 3, 4, and 5) because the volume density of synapses in the CA1 stratum radiatum is ~2 μm<sup>-3</sup> (Rusakov and Kullmann, 1998). Therefore, probing perisynaptic glutamate handling at a small spine will, to some degree, cosample the perisynaptic environment of a nearby, unlabeled synapse, which for statistical reasons is likely larger, and vice versa for probing of a large spine. Thus, the spine size dependence of glutamate uptake is likely to be stronger than that detected here. It correlated best with the relative abundance of glutamate transporters or astrocyte volume at small and large spines in ExM experiments (Figures 1 and 2). It is straightforward to imagine that the higher amount of surface GLT-1 relative to spine size (i.e., local GLT-1 density) at small spines (Figure 1) shields them better from distant glutamate sources (Figure 4) and leads to stronger increases of local glutamate transients (Figure 3) and NMDAR-mediated Ca2+ transients (Figure 5) at these spines after inhibition of glutamate uptake. But, although differences of the relative abundance of astrocytic GLT-1 are an intuitive explanation of the size dependence of glutamate uptake, a causal relationship remains to be established. Future work could, for instance, test if an experimentally induced rapid reduction or displacement of GLT-1 has a stronger effect on glutamate dynamics at smaller spines.

Our observation of a spine size dependence of glutamate uptake also adds to the recently emerging notion that glutamate uptake and glutamate transporter localization are regulated on more levels and in a more complex manner than previously appreciated. The deletion of the gap junction protein connexin 30, for instance, resulted in the invasion of the synaptic cleft by astrocyte processes, increased glutamate uptake, and decreased excitatory synaptic transmission (Pannasch et al., 2014). In addition, the mobility of the glutamate transporter GLT-1 on the astrocyte surface has recently been shown to be particularly high and activity and location dependent (Murphy-Royal et al., 2015), which adds another layer of complexity to astrocyte glutamate uptake. Similarly, glutamate uptake is modulated rapidly by burst-like neuronal activity in the cortex (Armbruster et al., 2016) and, more subtle, on a longer timescale of half an hour by pharmacological PAR1 activation in the hippocampus (Sweeney et al., 2017). Furthermore, the activity-dependence of glutamate uptake differs between brain regions (Romanos et al., 2019). We demonstrate that such variability and local adaptation of glutamate uptake can also be found at the level of single synapses.

#### Functional Significance of Spine-Size-Dependent Glutamate Uptake

At Schaffer collateral synapses, a reduction of glutamate uptake has been shown to increase synaptic crosstalk by GluN2B-containing NMDARs (Scimemi et al., 2004), i.e., it increases the probability of synaptically released glutamate to act on NMDARs at inactive synapses. Similarly, Monte Carlo simulations of synaptic glutamate signaling indicate that removing perisynaptic glutamate uptake increases the activation of perisynaptic NMDARs by synaptically released glutamate (Zheng et al., 2008). Thus, our results suggest that at large postsynaptic spines, released glutamate is more likely to activate perisynaptic NMDARs and to invade the extrasynaptic ECS. Because activation of GluN2B-containing, extrasynaptic NMDARs has been associated with the induction of long-term depression (LTD) (Liu et al., 2004; Papouin et al., 2012), our results also suggest that synaptic plasticity at large spines could be biased toward LTD. At thin spines, the relatively stronger local glutamate uptake is instead likely to confine glutamate signaling more strongly to synaptic GluN2A-containing NMDARs, thus favoring long-term potentiation (LTP) (Papouin et al., 2012). However, there has been a considerable debate about the association between NMDAR subunit composition and the direction of long-term plasticity (Morishita et al., 2007; Shipton and Paulsen, 2013). Exploring if the localization of NMDARs influences the direction and magnitude of synaptic plasticity independently of subtype composition could provide further insights. It is interesting in that regard that increasing GLT-1 expression by ceftriaxone was indeed reported to impair LTD at hippocampal mossy fiber synapses (Omrani et al., 2009).

A stronger glutamate uptake around small spines shields them and their high-affinity NMDARs better from glutamate spilling in from neighboring synapses (Figures 4 and 5). This may prevent activation of their NMDARs and induction of synaptic plasticity when nearby synapses are active. From the perspective of a small spine, its neighbors are likely to be large and, because of the positive correlation of spine size, presynaptic bouton volume, active zone area, and release probability (Holderith et al., 2012; Matz et al., 2010; Murthy et al., 2001; Schikorski and Stevens, 1997), their presynaptic terminals are more likely to release glutamate during presynaptic action potential firing. In this scenario, small spines would be preferentially shielded from their larger and more active neighboring synapses, provided that presynaptic action potential firing is similar and not compensating for the difference of release probability. Independent of these local variations in glutamate uptake and spread between synapses, the synaptically released glutamate is eventually mostly taken up by astrocytes. Therefore, the basic relationship between the amount of released glutamate across the many thousands of synapses within the territory of a single astrocyte and the transporter current recorded at the astrocyte cell body (Diamond et al., 1998; Lüscher et al., 1998) is unaffected by our observations.

The decrease of local glutamate uptake with increasing spine size also indicates that spine growth/shrinkage could be accompanied by changes of local glutamate uptake. Interestingly, induction of LTP is a potent trigger for both acute spine growth (Matsuzaki et al., 2004) and also for changes of perisynaptic astrocyte process motility and structure (Bernardinelli et al., 2014; Perez-Alvarez et al., 2014; Wenzel et al., 1991). Such plasticity-associated structural changes of perisynaptic astrocyte branches are, therefore, expected to modify local glutamate uptake.

The strength of local glutamate uptake could also determine the probability of released glutamate to activate presynaptic

#### **Article**



glutamate receptor either at the same or a neighboring synapse. Experiments in the supraoptic nucleus revealed, for instance, that a low coverage of neurons by astrocytes in lactating animals is associated with reduced glutamate uptake and stronger tonic activation of presynaptic metabotropic glutamate receptors (mGluRs) (Oliet et al., 2001). Accordingly, recruitment of presynaptic mGluRs at Schaffer collateral synapses could be more prominent near large postsynaptic spines. Thus, the gradual decrease of perisynaptic glutamate uptake efficiency with increasing postsynaptic spine size represents a rule that could also govern other aspects of synaptic neuron-astrocyte interactions.

Whether the present observations at hippocampal CA3-CA1 synapses also apply to other synapse populations and brain regions remains to be established. Future studies could also explore the functional relevance of different astrocytic coverage of distinct synaptic pathways, as documented, for example, in the cerebellum (Xu-Friedman et al., 2001).

#### **STAR**\*METHODS

Detailed methods are provided in the online version of this paper and include the following:

- KEY RESOURCES TABLE
- RESOURCE AVAILABILITY
  - Lead Contact
  - Materials Availability
  - Data and Code Availability
- EXPERIMENTAL MODEL AND SUBJECT DETAILS
- METHOD DETAILS
  - Expansion microscopy of spine coverage by GLT-1
  - $\, \bigcirc \,$  ExM analysis of the perisynaptic astrocytic volume
  - O Stereotactic injections
  - O Preparation of acute brain slices
  - O Glutamate imaging using iGluSnFR
  - O Glutamate uncaging on CA1 pyramidal cell spines
  - Glutamate iontophoresis and Ca<sup>2+</sup> imaging
- QUANTIFICATION AND STATISTICAL ANALYSIS

#### SUPPLEMENTAL INFORMATION

Supplemental Information can be found online at https://doi.org/10.1016/j.celrep.2020.108182.

#### **ACKNOWLEDGMENTS**

The glutamate sensor iGluSnFR was kindly provided by Loren L. Looger (Janelia Farm Research Campus, Howard Hughes Medical Institute). We thank Dmitri A. Rusakov (London) for helpful comments on a previous version of the manuscript. Research was supported by the Human Frontiers Science Program (HFSP; RGY0084/2012 to C.H. and C.J.J.), the German Academic Exchange Service (DAAD-Go8) Travel Fellowship (to C.H. and C.J.J.), the NRW-Rückkehrerprogramm (C.H.), and German Research Foundation (DFG; SFB1089 B03, SPP1757 HE6949/1, FOR2795, and HE6949/3 to C.H.; SPP1757 young investigator grant to M.K.H.; SFB1089 P03 to M.K.S.; and SFB1089 B03, SPP1757 DI853/5, DI853/3, DI853/4, and DI853/7 to D.D.).

#### **AUTHOR CONTRIBUTIONS**

M.K.H. and S.P. performed glutamate imaging experiments. K.B. did all Ca<sup>2+</sup> imaging. M.K.S., M.K.H., C.D., and J.A.K.-M. established and performed

expansion microscopy. N.V. and D.D. performed and analyzed glutamate uncaging experiments. C.H. designed the study, analyzed data, and together with M.K.H. wrote the initial manuscript, to which then all authors contributed.

#### **DECLARATION OF INTERESTS**

The authors declare no competing interests.

Received: April 28, 2017 Revised: August 12, 2020 Accepted: September 1, 2020 Published: September 22, 2020

#### **REFERENCES**

Anders, S., Minge, D., Griemsmann, S., Herde, M.K., Steinhäuser, C., and Henneberger, C. (2014). Spatial properties of astrocyte gap junction coupling in the rat hippocampus. Philos. Trans. R. Soc. Lond. B Biol. Sci. *369*, 20130600

Arizono, M., Inavalli, V.V.G.K., Panatier, A., Pfeiffer, T., Angibaud, J., Levet, F., Veer, M.J.T.T., Stobart, J., Bellocchio, L., Mikoshiba, K., et al. (2020). Structural basis of astrocytic Ca 2+ signals at tripartite synapses. Nat. Commun. 11, 1–15

Armbruster, M., Hanson, E., and Dulla, C.G. (2016). Glutamate Clearance Is Locally Modulated by Presynaptic Neuronal Activity in the Cerebral Cortex. J. Neurosci. *36*, 10404–10415.

Asano, S.M., Gao, R., Wassie, A.T., Tillberg, P.W., Chen, F., and Boyden, E.S. (2018). Expansion Microscopy: Protocols for Imaging Proteins and RNA in Cells and Tissues. Curr. Protoc. Cell Biol. 80, e56.

Bartol, T.M., Jr., Bromer, C., Kinney, J., Chirillo, M.A., Bourne, J.N., Harris, K.M., and Sejnowski, T.J. (2015). Nanoconnectomic upper bound on the variability of synaptic plasticity. eLife *4*, e10778.

Bernardinelli, Y., Randall, J., Janett, E., Nikonenko, I., König, S., Jones, E.V., Flores, C.E., Murai, K.K., Bochet, C.G., Holtmaat, A., and Muller, D. (2014). Activity-dependent structural plasticity of perisynaptic astrocytic domains promotes excitatory synapse stability. Curr. Biol. 24, 1679–1688.

Cavelier, P., and Attwell, D. (2005). Tonic release of glutamate by a DIDS-sensitive mechanism in rat hippocampal slices. J. Physiol. *564*, 397–410.

Chen, F., Tillberg, P.W., and Boyden, E.S. (2015). Optical imaging. Expansion microscopy. Science *347*, 543–548.

Chozinski, T.J., Halpern, A.R., Okawa, H., Kim, H.-J., Tremel, G.J., Wong, R.O.L., and Vaughan, J.C. (2016). Expansion microscopy with conventional antibodies and fluorescent proteins. Nat. Methods *13*, 485–488.

Cull-Candy, S.G., and Leszkiewicz, D.N. (2004). Role of distinct NMDA receptor subtypes at central synapses. Sci. STKE 2004, re16.

Danbolt, N.C. (2001). Glutamate uptake. Prog. Neurobiol. 65, 1–105.

Diamond, J.S., Bergles, D.E., and Jahr, C.E. (1998). Glutamate release monitored with astrocyte transporter currents during LTP. Neuron *21*, 425–433.

Feng, G., Mellor, R.H., Bernstein, M., Keller-Peck, C., Nguyen, Q.T., Wallace, M., Nerbonne, J.M., Lichtman, J.W., and Sanes, J.R. (2000). Imaging neuronal subsets in transgenic mice expressing multiple spectral variants of GFP. Neuron 28. 41–51.

Gavrilov, N., Golyagina, I., Brazhe, A., Scimemi, A., Turlapov, V., and Semyanov, A. (2018). Astrocytic Coverage of Dendritic Spines, Dendritic Shafts, and Axonal Boutons in Hippocampal Neuropil. Front. Cell. Neurosci. *12*, 248.

Genoud, C., Quairiaux, C., Steiner, P., Hirling, H., Welker, E., and Knott, G.W. (2006). Plasticity of astrocytic coverage and glutamate transporter expression in adult mouse cortex. PLoS Biol. *4*, e343.

Godin, A.G., Varela, J.A., Gao, Z., Danné, N., Dupuis, J.P., Lounis, B., Groc, L., and Cognet, L. (2017). Single-nanotube tracking reveals the nanoscale organization of the extracellular space in the live brain. Nat. Nanotechnol. *12*, 238–243.



Harris, K.M., and Stevens, J.K. (1989). Dendritic spines of CA 1 pyramidal cells in the rat hippocampus: serial electron microscopy with reference to their biophysical characteristics. J. Neurosci. 9, 2982-2997.

Heller, J.P., and Rusakov, D.A. (2015). Morphological plasticity of astroglia: Understanding synaptic microenvironment. Glia 63, 2133-2151.

Helmchen, F., and Denk, W. (2005). Deep tissue two-photon microscopy. Nat. Methods 2, 932-940.

Holderith, N., Lorincz, A., Katona, G., Rózsa, B., Kulik, A., Watanabe, M., and Nusser, Z. (2012). Release probability of hippocampal glutamatergic terminals scales with the size of the active zone. Nat. Neurosci. 15, 988-997.

Holmseth, S., Dehnes, Y., Huang, Y.H., Follin-Arbelet, V.V., Grutle, N.J., Mylonakou, M.N., Plachez, C., Zhou, Y., Furness, D.N., Bergles, D.E., et al. (2012). The density of EAAC1 (EAAT3) glutamate transporters expressed by neurons in the mammalian CNS. J. Neurosci. 32, 6000-6013.

Korogod, N., Petersen, C.C., and Knott, G.W. (2015). Ultrastructural analysis of adult mouse neocortex comparing aldehyde perfusion with cryo fixation. eLife

Le Meur, K., Galante, M., Angulo, M.C., and Audinat, E. (2007). Tonic activation of NMDA receptors by ambient glutamate of non-synaptic origin in the rat hippocampus. J. Physiol. 580, 373-383.

Liu, L., Wong, T.P., Pozza, M.F., Lingenhoehl, K., Wang, Y., Sheng, M., Auberson, Y.P., and Wang, Y.T. (2004). Role of NMDA receptor subtypes in governing the direction of hippocampal synaptic plasticity. Science 304, 1021–1024.

Lüscher, C., Malenka, R.C., and Nicoll, R.A. (1998). Monitoring glutamate release during LTP with glial transporter currents. Neuron 21, 435-441.

Lushnikova, I., Skibo, G., Muller, D., and Nikonenko, I. (2009). Synaptic potentiation induces increased glial coverage of excitatory synapses in CA1 hippocampus. Hippocampus 19, 753-762.

Marvin, J.S., Borghuis, B.G., Tian, L., Cichon, J., Harnett, M.T., Akerboom, J., Gordus, A., Renninger, S.L., Chen, T.-W., Bargmann, C.I., et al. (2013). An optimized fluorescent probe for visualizing glutamate neurotransmission. Nat. Methods 10, 162-170.

Matsuzaki, M., Ellis-Davies, G.C., Nemoto, T., Miyashita, Y., Iino, M., and Kasai, H. (2001). Dendritic spine geometry is critical for AMPA receptor expression in hippocampal CA1 pyramidal neurons. Nat. Neurosci. 4, 1086-1092.

Matsuzaki, M., Honkura, N., Ellis-Davies, G.C.R., and Kasai, H. (2004). Structural basis of long-term potentiation in single dendritic spines. Nature 429, 761-766.

Matz, J., Gilyan, A., Kolar, A., McCarvill, T., and Krueger, S.R. (2010). Rapid structural alterations of the active zone lead to sustained changes in neurotransmitter release. Proc. Natl. Acad. Sci. USA 107, 8836-8841.

Medvedev, N., Popov, V., Henneberger, C., Kraev, I., Rusakov, D.A., and Stewart, M.G. (2014). Glia selectively approach synapses on thin dendritic spines. Philos. Trans. R. Soc. Lond. B Biol. Sci. 369, 20140047.

Minge, D., Senkov, O., Kaushik, R., Herde, M.K., Tikhobrazova, O., Wulff, A.B., Mironov, A., van Kuppevelt, T.H., Oosterhof, A., Kochlamazashvili, G., et al. (2017). Heparan Sulfates Support Pyramidal Cell Excitability, Synaptic Plasticity, and Context Discrimination. Cereb. Cortex 27, 903-918.

Morishita, W., Lu, W., Smith, G.B., Nicoll, R.A., Bear, M.F., and Malenka, R.C. (2007). Activation of NR2B-containing NMDA receptors is not required for NMDA receptor-dependent long-term depression. Neuropharmacology 52, 71-76

Murphy-Royal, C., Dupuis, J.P., Varela, J.A., Panatier, A., Pinson, B., Baufreton, J., Groc, L., and Oliet, S.H.R. (2015). Surface diffusion of astrocytic glutamate transporters shapes synaptic transmission. Nat. Neurosci. 18, 219-226.

Murthy, V.N., Schikorski, T., Stevens, C.F., and Zhu, Y. (2001). Inactivity produces increases in neurotransmitter release and synapse size. Neuron 32, 673-682.

Nolte, C., Matyash, M., Pivneva, T., Schipke, C.G., Ohlemeyer, C., Hanisch, U.K., Kirchhoff, F., and Kettenmann, H. (2001). GFAP promoter-controlled EGFP-expressing transgenic mice: a tool to visualize astrocytes and astrogliosis in living brain tissue. Glia 33, 72-86.

Octeau, J.C., Chai, H., Jiang, R., Bonanno, S.L., Martin, K.C., and Khakh, B.S. (2018). An Optical Neuron-Astrocyte Proximity Assay at Synaptic Distance Scales. Neuron 98, 49-66.e9.

Oliet, S.H., Piet, R., and Poulain, D.A. (2001). Control of glutamate clearance and synaptic efficacy by glial coverage of neurons. Science 292, 923-926.

Omrani, A., Melone, M., Bellesi, M., Safiulina, V., Aida, T., Tanaka, K., Cherubini, E., and Conti, F. (2009). Up-regulation of GLT-1 severely impairs LTD at mossy fibre-CA3 synapses. J. Physiol. 587, 4575-4588.

Pannasch, U., Freche, D., Dallérac, G., Ghézali, G., Escartin, C., Ezan, P., Cohen-Salmon, M., Benchenane, K., Abudara, V., Dufour, A., et al. (2014). Connexin 30 sets synaptic strength by controlling astroglial synapse invasion. Nat. Neurosci. 17, 549-558.

Papouin, T., Ladépêche, L., Ruel, J., Sacchi, S., Labasque, M., Hanini, M., Groc, L., Pollegioni, L., Mothet, J.-P., and Oliet, S.H.R. (2012). Synaptic and extrasynaptic NMDA receptors are gated by different endogenous coagonists. Cell 150, 633-646.

Patrushev, I., Gavrilov, N., Turlapov, V., and Semyanov, A. (2013). Subcellular location of astrocytic calcium stores favors extrasynaptic neuron-astrocyte communication. Cell Calcium 54, 343-349.

Perez-Alvarez, A., Navarrete, M., Covelo, A., Martin, E.D., and Araque, A. (2014). Structural and functional plasticity of astrocyte processes and dendritic spine interactions. J. Neurosci. 34, 12738-12744.

Protopapas, A.D., Vanier, M., and Bower, J.M. (1998). Simulating large networks of neurons. Methods in Neuronal Modeling: From Ions to Networks (MIT Press), p. 461.

Romanos, J., Benke, D., Saab, A.S., Zeilhofer, H.U., and Santello, M. (2019). Differences in glutamate uptake between cortical regions impact neuronal NMDA receptor activation. Commun. Biol. 2, 127.

Rose, C.R., Felix, L., Zeug, A., Dietrich, D., Reiner, A., and Henneberger, C. (2018). Astroglial Glutamate Signaling and Uptake in the Hippocampus. Front. Mol. Neurosci. 10, 451.

Rosenmund, C., and Westbrook, G.L. (1993). Rundown of N-methyl-D-aspartate channels during whole-cell recording in rat hippocampal neurons: role of Ca2+ and ATP. J. Physiol. 470, 705-729.

Rusakov, D.A., and Kullmann, D.M. (1998). Extrasynaptic glutamate diffusion in the hippocampus: ultrastructural constraints, uptake, and receptor activation. J. Neurosci. 18, 3158-3170.

Schikorski, T., and Stevens, C.F. (1997). Quantitative ultrastructural analysis of hippocampal excitatory synapses. J. Neurosci. 17, 5858-5867.

Scimemi, A., Fine, A., Kullmann, D.M., and Rusakov, D.A. (2004). NR2B-containing receptors mediate cross talk among hippocampal synapses. J. Neurosci. 24, 4767-4777.

Sheng, M., and Hoogenraad, C.C. (2007). The postsynaptic architecture of excitatory synapses: a more quantitative view. Annu. Rev. Biochem. 76, 823-847

Shipton, O.A., and Paulsen, O. (2013). GluN2A and GluN2B subunit-containing NMDA receptors in hippocampal plasticity. Philos. Trans. R. Soc. Lond. B Biol. Sci. 369, 20130163.

Smith, M.A., Ellis-Davies, G.C., and Magee, J.C. (2003). Mechanism of the distance-dependent scaling of Schaffer collateral synapses in rat CA1 pyramidal neurons. J. Physiol. 548, 245-258.

Sun, W., Matthews, E.A., Nicolas, V., Schoch, S., and Dietrich, D. (2016). NG2 glial cells integrate synaptic input in global and dendritic calcium signals. eLife 5. e16262.

Sweeney, A.M., Fleming, K.E., McCauley, J.P., Rodriguez, M.F., Martin, E.T., Sousa, A.A., Leapman, R.D., and Scimemi, A. (2017). PAR1 activation induces rapid changes in glutamate uptake and astrocyte morphology. Sci. Rep. 7,

Syková, E., and Nicholson, C. (2008). Diffusion in brain extracellular space. Physiol. Rev. 88, 1277-1340.

## **Article**



Tønnesen, J., Inavalli, V.V.G.K., and Nägerl, U.V. (2018). Super-Resolution Imaging of the Extracellular Space in Living Brain Tissue. Cell 172, 1108-1121.e15.

Ventura, R., and Harris, K.M. (1999). Three-dimensional relationships between hippocampal synapses and astrocytes. J. Neurosci. 19, 6897-6906.

Wenzel, J., Lammert, G., Meyer, U., and Krug, M. (1991). The influence of longterm potentiation on the spatial relationship between astrocyte processes and potentiated synapses in the dentate gyrus neuropil of rat brain. Brain Res. 560, 122-131.

Witcher, M.R., Kirov, S.A., and Harris, K.M. (2007). Plasticity of perisynaptic astroglia during synaptogenesis in the mature rat hippocampus. Glia 55, 13-23.

Witcher, M.R., Park, Y.D., Lee, M.R., Sharma, S., Harris, K.M., and Kirov, S.A. (2010). Three-dimensional relationships between perisynaptic astroglia and human hippocampal synapses. Glia 58, 572-587.

Xu-Friedman, M.A., Harris, K.M., and Regehr, W.G. (2001). Three-dimensional comparison of ultrastructural characteristics at depressing and facilitating synapses onto cerebellar Purkinje cells. J. Neurosci. 21, 6666-6672.

Zhang, W.H., Herde, M.K., Mitchell, J.A., Whitfield, J.H., Wulff, A.B., Vongsouthi, V., Sanchez-Romero, I., Gulakova, P.E., Minge, D., Breithausen, B., et al. (2018). Monitoring hippocampal glycine with the computationally designed optical sensor GlyFS. Nat. Chem. Biol. 14, 861-869.

Zheng, K., Scimemi, A., and Rusakov, D.A. (2008). Receptor actions of synaptically released glutamate: the role of transporters on the scale from nanometers to microns. Biophys. J. 95, 4584-4596.





## **STAR**\*METHODS

#### **KEY RESOURCES TABLE**

REAGENT or RESOURCE	SOURCE	IDENTIFIER
Antibodies	GOGNOL	IDENTIFICATION OF THE PROPERTY
chicken anti GFP	Abcam	ab13970; RRID:AB 300798
guinea-pig anti GLT-1	Millipore	AB1783; RRID:AB_90949
rabbit anti GLAST	Abcam	ab416; RRID:AB_304334
goat anti chicken Alexa Fluor 488	ThermoFisher	A11039; RRID:AB_2534096
goat anti guinea-pig Alexa Fluor 568 or 594	ThermoFisher	A11075; RRID:AB_2534119 or A11076; RRID:AB_2534120
goat anti rabbit biotin	Jackson ImmunoResearch	111-066-144; RRID:AB_2337970
guinea-pig anti-Shank2	Synaptic Systems	162 204; RRID:AB_2619861
mouse anti Bassoon	Enzo	SAP7F407; RRID:AB_10618753
goat anti mouse biotin	Jackson ImmunoResearch	115-067-003; RRID:AB_2338586
Bacterial and Virus Strains		
AAV GFAP-iGluSnFR	PennCore	AAV1.GFAP.iGluSnFr.WPRE.SV40
Chemicals, Peptides, and Recombinant Proteins		
Tetrodotoxin	Tocris	Cat. #1069
Nifedipine	Sigma-Aldrich	Cat. #N7634
LY341495	Tocris	Cat. #4062
MPEP	Abcam	Cat. ab120008
TFB-TBOA	Tocris	Cat. #2532
D-APV	Abcam	Cat. ab120003
Alexa Fluor 594 Hydrazide	ThermoFisher	Cat. A10438
Fluo-4, pentapotassium salt	ThermoFisher	Cat. F14200
NBQX	Abcam	Cat. ab120046
MNI-caged-L-glutamate	Tocris	Cat. #1490
Experimental Models: Organisms/Strains		
C57BL6/N mice	Charles River	Strain Code 027
Wistar rats	Charles River	Strain Code 003
Thy1-YFP mice	Feng et al., 2000	N/A
GFAP-EGFP mice	Nolte et al., 2001	N/A
Software and Algorithms		
Custom imaging data analysis scripts	This manuscript	N/A

## **RESOURCE AVAILABILITY**

#### **Lead Contact**

Further information and requests for resources and reagents should be directed to and will be fulfilled by the Lead Contact, Christian Henneberger (christian.henneberger@uni-bonn.de).

#### **Materials Availability**

This study did not generate new unique reagents.

#### **Data and Code Availability**

The data supporting the current study and custom code have not yet been deposited in a public repository because of their highly diverse nature and formats but are available from the lead contact on request. Original/source data for figures in the paper are also available on request.

# **Cell Reports Article**



#### **EXPERIMENTAL MODEL AND SUBJECT DETAILS**

All animal procedures were conducted in accordance with the regulations of the European Commission and all relevant national and institutional guidelines and requirements. Procedures have been approved by the Landesamt für Natur, Umwelt und Verbraucherschutz Nordrhein-Westfalen (LANUV, Germany) where required.

All animals used in this study were housed under 12 h light/dark conditions and were allowed ad libitum access to food and water. For expansion microscopy, male and female Thy1-YFP mice (Feng et al., 2000) or male and female GFAP-EGFP mice (Nolte et al., 2001), in which a subset of hippocampal astrocytes express EGFP, were sacrificed at an age of 7 to 10 weeks. iGluSnFR experiments were performed on 7 to 10-week-old male C57BL6/N mice (see below for virus injection procedure). Glutamate iontophoresis experiments were performed on 3-5 week-old male Wistar rats. For glutamate uncaging experiments, male C57BL/6J mice between 26 and 44 days of age were used. All experiments were performed in the stratum radiatum of the CA1 region of the hippocampus.

#### **METHOD DETAILS**

#### **Expansion microscopy of spine coverage by GLT-1**

The expansion microscopy (ExM) technique was adopted from the literature (Asano et al., 2018; Chen et al., 2015; Chozinski et al., 2016). Thy1-YFP mice were deeply anesthetized and transcardially perfused with 4% paraformaldehyde in phosphate buffered saline (PBS, pH 7.4). Brains were removed from the skull, postfixed for 1-2 h at 4°C before being stored in PBS. Coronal sections of 70 µm thickness were cut on a vibratome and blocked for 6 h at room temperature (RT) in blocking buffer (5% normal goat serum, 0.1% Triton X-100 in PBS). Primary antibodies were incubated in blocking buffer for 48 h at 4°C. Antibodies used were: chicken anti GFP (1:5000; Abcam ab13970, lot GR89472-16), guinea-pig anti GLT-1 (1:500; Millipore AB1783, lot 2572967), rabbit anti GLAST (1:200; Abcam ab416, lot GR266539-1). After 3x20 min washing in blocking buffer, samples were incubated with secondary antibodies at 4°C for 12 h. Secondary antibodies used were: goat anti chicken Alexa Fluor 488 (1:200; ThermoFisher A11039), goat anti guinea-pig Alexa Fluor 568 or 594 (1:200; ThermoFisher A11075 or A11076), goat anti rabbit biotin (1:400; Jackson ImmunoResearch 111-066-144). After washing in blocking buffer, slices were pre-expansion imaged in PBS containing 0.05% p-phenyldiamine. Further treatment was adopted from Chen et al. (2015) and Chozinski et al. (2016). Briefly, slices were incubated in 1 mM methylacrylic acid-NHS (Sigma Aldrich #730300) at RT for 1 h. After washing, slices were incubated for 45 min in monomer solution (in g/100 mL PBS: 8.6 sodium acrylate, 2.5 acrylamide, 0.15 N,N'-methylenebisacrylamide, 11.7 NaCl) at 4°C. Then, slices were incubated with gelling solution (monomer solution supplemented with %(w/v): 0.01 4-hydroxy-TEMPO, 0.2 TEMED, 0.2 APS) at 4°C for 5 min before transferring them to a chamber sandwiched between coverslips at 37°C for 2 h. Coverslips were removed and proteins were digested in digestion buffer (50 mM Tris pH 8, 1 mM EDTA, 0.5% Triton X-100, 0.8 M guanidine, 16 U/ml proteinase K) at 37°C for 12-14 h. For a triple label (Figure S2), slices were incubated with streptavidin Alexa Fluor 647 (1:1000; Jackson ImmunoResearch 016-600-084) in PBS with 3% bovine serum albumine at RT for 1 h. For expansion, slices were then incubated for 2.5 h in distilled water and water was exchanged repeatedly every 15-20 min. Finally, slices were transferred to a custom mounting chamber filled with distilled water, mounted by superglueing its edges to the chamber's bottom and sealed with a coverslip on the top. Image stacks were acquired on a Leica SP8 confocal microscope using a 40x/1.1NA water immersion objective and hybrid detectors (pixel dimension x-y plane  $90 \times 90 \text{ nm}^2$ , z-steps 426 nm, typical stack size x-y-z of  $1000 \times 1000 \times 70 \text{ voxels}$ ). The expansion factor was determined by measuring gel sizes before and after expansion. On average, we measured an expansion factor of 4.55 ± 0.05 (n = 9). An upper limit of the spatial resolution obtainable by expansion microscopy was established using a punctate staining against Homer1 (see Figure S1). Using expansion microscopy, we could resolve Homer1 puncta as small as ~40 nm (x-y plane) and ~270 nm (z-plane). This is in line with previous reports (Chen et al., 2015; Chozinski et al., 2016). Images were deconvolved using Huygens Essential and analyzed in 3D with FIJI, Elastix and custom-written software (Chozinski et al., 2016).

GLT-1 coverage of dendritic spines of hippocampal CA1 pyramidal cells was analyzed by using the RG2B colocalization tool of ImageJ. Coverage was determined by counting voxels positive for GLT-1 and YFP in spherical volumes of interest with varying radii. The volume of interest was centered on the spine's center of mass of YFP fluorescence. A measure of relative GLT-1 coverage was obtained by normalizing this pixel count to the spine volume. This analysis was performed in spheres of interest with three diameters (0.42  $\mu$ m, 0.50  $\mu$ m, 0.65  $\mu$ m, see Figure 1 and Results). Also see Quantification and Statistical Analysis below for further

The spine volume was obtained from Z axis profiles of spine YFP fluorescence. Z-profiles of the average intensity in square regions of interest ( $\sim$ 1 × 1  $\mu$ m<sup>2</sup> real size,  $\sim$ 4 × 4  $\mu$ m<sup>2</sup> post-expansion) centered on the spine were plotted for each individual spine. The area under the curve of each profile was fitted by a Gaussian function and used as a measure of spine volume. This measure of spine volume was used instead of, for instance, threshold-based volume or surface renderings because it can be readily obtained from both ExM and two-photon excitation microscopy data (see below), it is relatively insensitive to the optical resolution and it does not require setting a threshold. To account for varying YFP expression levels between cells and varying imaging conditions between experiments, individual spine volumes were normalized to the median volume of neighboring spines on the same dendritic segment. We used the median because spine volumes were often not normally distributed in these experiments. Individual spines were categorized as 'small' or 'large' if their volume was below or above, respectively, this median spine volume.





#### ExM analysis of the perisynaptic astrocytic volume

Brain perfusion and fixation of GFAP-EGFP mice were performed as described above, with an overnight post-fixation period. Coronal hippocampal slices (70 µm thickness) were cut on a vibratome and blocked overnight (ON) at 4°C in permeabilization buffer (0.5% Triton X-100 in PBS pH 7.4). Antibodies were incubated individually for 24 h at 4°C in permeabilization buffer (0.5% Triton X-100 in PBS) if not otherwise stated. In between antibody incubations, slices were washed in PBS 3x20 min at RT. Primary antibodies: chicken anti GFP (1:5000; Abcam ab13970, lot GR236651-g), guinea-pig anti-Shank2 (1:100; Synaptic Systems 162 204), mouse anti Bassoon (1:100; Enzo SAP7F407, lot 06231712). Secondary antibodies: goat anti chicken Alexa Fluor 488 (1:200; ThermoFisher A11039, lot 1899519), goat anti guinea pig Alexa Fluor 568 (1:200; ThermoFisher A11075, lot 1692965), goat anti mouse biotin (1:200; Jackson ImmunoResearch 115-067-003, lot 130148). After washing in PBS, slices were incubated with Hoechst 33342 (1:2000, Invitrogen H3570, lot 1874027) in distilled water for 10 min at RT. After washing again, slices were imaged in PBS before expansion with a 20x/0.75 NA objective in a Leica SP8 confocal microscope. ExM was performed as described above (see also Asano et al., 2018, section Basic ProExM protocol for intact tissues), with the following modifications. Incubation with the linker methylacrylic acid-NHS, gelling and digestion steps were performed as described above, except digestion occurred at 25°C for 12-14 h. After digestion, slices were incubated with streptavidin Alexa Fluor 647 (1:200; Jackson ImmunoResearch 016-600-084, lot 124695) in PBS at RT for 2 h. For expansion, slices were then incubated in distilled water (adjusted pH 7.4 with NaOH) for 2.5 h at RT and water exchanged repeatedly every 15-20 min. Finally, slices were mounted on poly-lysine coated  $\mu$ -Slide 2 well Ibidi-chambers and sealed with a poly-lysine coated coverslip on top, adding a drop of water to prevent the gel from drying. µ-Slide 2 Ibidi chambers and coverslips were polylysine coated by incubation with poly-I-lysine solution (0.01% w/v in water (P8920, Sigma-Aldrich, lot: 050M4339) for at least 45 min at RT shaking and dried with pressured air.

Fluorescence microscopy was performed on a Leica SP8 inverted confocal microscope using a 40x/1.1NA objective and hybrid detectors. For each sample, the expansion factor was determined by identifying the same cells labeled with Hoechst 33342 in the dentate gyrus before and after expansion and then measuring their sizes pre- and post-expansion. The expansion factor of an individual sample was then calculated as the average ratio of post- and pre-expansion sizes of  $\sim$ 10 measures from the same sample. On average, we obtained an expansion factor of 4.61 ± 0.18 (n = 4) in these experiments. For analysis, image stacks of astrocytes (EGFP) and covered pre- and postsynaptic structures (Bassoon and Shank2) were acquired (x-y-z, typically ~2500 × 2500 × 15 voxels, voxel dimensions  $\sim$ 0.1  $\mu$ m x 0.1  $\mu$ m x 0.4  $\mu$ m, corresponding to pre-expansion dimensions of  $\sim$ 0.02  $\mu$ m x 0.02  $\mu$ m x 0.09  $\mu$ m). Image stacks were then deconvolved in Leica Systems software and further processed with FIJI and MATLAB.

Individual putative single synaptic contacts were identified by direct apposition of pre- and post-synaptic labeling (bassoon and shank2, respectively) within the astrocyte territory (without inspection of their astrocytic 3D coverage to avoid a selection bias). 3D volumes of interest of putative single synaptic contacts were obtained by cropping a volume of 1.5 × 1.5 × 1.5 μm<sup>3</sup> centered on the center of mass of post-synaptic shank2 fluorescence, i.e., the post-synaptic density (PSD). The PSD volume was then calculated as the cumulative fluorescence intensity of shank2, measured in a rectangular volume of interest centered and exclusively containing the post-synaptic domain. For each analyzed astrocyte, PSDs were categorized as 'small' or 'large' if their volume was below or above, respectively, the median PSD volume for that astrocyte. For each synaptic contact, the distribution of astrocytic EGFP fluorescence was quantified in 3D after background subtraction. This analysis was performed by determining the astroglial EGFP fluorescence in spherical shells with a thickness of 20 nm and increasing diameter (see Figure 2 for an illustration) centered on the shank2 label (PSD center of mass as above). For each shell, the sum and average of EGFP fluorescence intensity was determined. For each astrocyte, profiles of EGFP intensity over distance at small and large PSDs were averaged, both for the sum and for the average of EGFP fluorescence. From these, the population averages and SEM across all astrocytes were calculated (Figures 2B and 2C). For other analyses (Figures 2D and 2E), the cumulative EGFP fluorescence across all shells was obtained, averaged for small and large PSDs in each astrocyte (paired data) and then compared across individual astrocytes.

#### Stereotactic injections

For the expression of the glutamate sensor iGluSnFR (Marvin et al., 2013) in astrocytes, an AAV virus expressing iGluSnFR under a GFAP promoter (AAV1.GFAP.iGluSnFr.WPRE.SV40, PennCore) was injected bilaterally into the ventral hippocampus. C57BL6/N mice (4 weeks old, Charles Rivers Laboratories) were injected intra-peritoneally (i.p.) with a ketamin/medotomidine anesthesia (100 and 0.25 mg per kg body weight in NaCl, injection volume 0.1 mL per 10 g body weight, ketamin 10%, betapharm; Cepotir 1 mg/ml, CPPharma). First, the head fur was removed and the underlying skin disinfected. After ensuring that the animal was under deep anesthesia, the head was fixed in a stereotactic frame (Model 901, David Kopf Instruments). After making an incision, bregma was localized. Next, the coordinates for the ventral hippocampus (relative to bregma: anterior -3.5 mm, lateral ± 3 mm, ventral -2.5 mm) were determined and the skull was locally opened with a dental drill. Under control of a micro injection pump (100 nl/min, WPI) 1 µl viral particles were injected with a beveled needle nanosyringe (nanofil 34G BVLD, WPI). After retraction of the syringe, the incision was sutured using absorbable thread (Ethicon). Finally, the anesthesia was stopped by i.p. injection of atipamezol (2.5 mg per kg body weight in NaCl, injection volume 0.1 mL per 10 g body weight, antisedan 5 mg/ml, Ventoquinol). To ensure analgesia, carprofen (5 mg/kg in NaCl, injection volume 0.1 ml/20 g body weight, Rimadyl 50 mg/ml, Zoetis) was injected subcutaneously directly, 24 h and 48 h after the surgery.

# **Cell Reports Article**



#### **Preparation of acute brain slices**

Preparation of acute hippocampal slices was performed as described previously (Anders et al., 2014; Minge et al., 2017; Zhang et al., 2018). Briefly, animals were deeply anesthetized with isoflurane, decapitated and 300 μm thick horizontal hippocampal slices were prepared in an ice-cold solution containing (in mM): NaCl 60, sucrose 105, KCl 2.5, MgCl<sub>2</sub> 7, NaH<sub>2</sub>PO<sub>4</sub> 1.25, ascorbic acid 1.3, sodium pyruvate 3, NaHCO<sub>3</sub> 26, CaCl<sub>2</sub> 0.5 and glucose 10 (osmolarity 305–310 mOsm). Slices were kept in slicing solution at 34°C for 15 min and then transferred to an artificial cerebrospinal fluid (ACSF) solution containing (in mM): NaCl 131, KCl 2.5, MgSO<sub>4</sub> 1.3, NaH<sub>2</sub>PO<sub>4</sub> 1.25, NaHCO<sub>3</sub> 21, CaCl<sub>2</sub> 2 and glucose 10 (pH 7.35-7.45; osmolarity adjusted to 297-303 mOsm) at RT. Slices were allowed to rest for at least 45 min at RT before experiments were started.

#### Glutamate imaging using iGluSnFR

Slices were transferred to a submersion-type recording chamber mounted on an Olympus FV10MP two-photon excitation (2PE) fluorescence microscope with a 25x/1.05NA objective and superfused with ACSF at 34°C. For the spine imaging experiments shown, a CA1 pyramidal neuron was briefly patched (5-10 min, using a Multiclamp 700B amplifier) with an intracellular solution containing (in mM): KCH<sub>3</sub>O<sub>3</sub>S 135, HEPES 10, di-Tris-Phosphocreatine 10, MgCl<sub>2</sub> 4, Na<sub>2</sub>-ATP 4, Na-GTP 0.4 Alexa Fluor hydrazide 0.2 (pH adjusted to 7.2 using KOH, osmolarity 290-295 mOsm). A dendritic segment with a variety of different apparent spine sizes and an iGluSnFR-expressing astrocyte (identified by their typical ramified morphology with fine processes) nearby was selected and an extracellular field electrode pulled from borosilicate glass (2-4  $\mathrm{M}\Omega$  resistance) was placed nearby. Then, a concentric bipolar stimulation electrode (FHC, CBARC75) was placed in the Schaffer collateral pathway  $\sim$ 200  $\mu m$  from the imaging site. iGluSnFR fluorescence responses to 100 Hz stimulation (for 100 ms, 70 μA intensity, 50 sweeps) were imaged at an 2PE wavelength of 910 nm using a femtosecond pulsed laser (Vision S, Coherent) and a photomultiplier tube connected to a single photon counting board (Picoharp with Symphotime software, Picoquant). Throughout the study, the laser power was adjusted so that the fluorescence intensity at the region of interest was equivalent to that obtained with imaging at 3 mW at the slice surface. The analysis of iGluSnFR transients in 1 µm2 ROIs around individual spines was performed offline using custom written MATLAB (Mathworks) scripts and Clampfit (Molecular Devices). The iGluSnFR fluorescence intensity over time was extracted from single photon counting data and corrected for excitation-independent photons, i.e., by subtracting for each time window the photon count that corresponds to the photon count rate measured with the laser shutter closed. Fluorescence intensity changes ( $\Delta F$ ) were normalized to the baseline fluo $rescence\ intensity\ (F_0).\ Experiments\ were\ excluded\ from\ analysis\ if\ the\ amplitudes\ of\ iGluSnFR\ fluorescence\ transients\ were\ <1.5\%$ ΔF/F<sub>0</sub>. Spine volumes were determined from stack images (z step 0.5 μm) through the dendritic segment and were analyzed as described for ExM (see above). Relative spine volumes were calculated normalizing to the median of 10 neighboring spines.

#### Glutamate uncaging on CA1 pyramidal cell spines

CA1 pyramidal cells in acute hippocampal slices (300 µm thick, see above for further details) were recorded from at RT. We used a combination of whole-cell recordings and two-photon uncaging of MNI-glutamate (Tocris) to elicit glutamatergic responses at single synapses of hippocampal CA1 pyramidal neurons (Matsuzaki et al., 2001; Smith et al., 2003; Sun et al., 2016). Cells were patched using borosilicate glass pipettes (3-6 MΩ) filled with an intracellular solution containing (in mM): 100 Cs-gluconate, 4 MgCl<sub>2</sub>, 4 ATP disodium salt, 0.5 EGTA, 10 HEPES, 30 CsCl, 5 QX-314 Bromide and 0.025 Alexa Fluor 594 (Thermo Fisher). To avoid evoking action potential-induced currents and to isolate NMDAR currents, the recording solution was supplemented with 1 µM TTX (Biotrend) and 10 μM CNQX (Tocris). Once a whole-cell configuration was established the perfusion was stopped and MNI-glutamate and D-serine (Sigma) were added directly to the recording chamber to achieve a final concentration of 5 mM and 100 μM respectively. D-serine was added to avoid a potential contribution of variable NMDAR co-agonist site occupancy to the results. MNI-glutamate uncaginginduced currents were recorded only between 10 and 25 minutes after drug application to ensure an equal concentration of the substances in the chamber, while maintaining cell viability. NMDAR-mediated currents were recorded at +40 mV holding potential upon photolysis of MNI-glutamate using a Prairie Technologies Ultima Multiphoton Microscopy System (Bruker) in combination with the Prairieview software controlling two Ti:sapphire lasers and two scan heads. The uncaging laser pulse (duration 0.6 ms, wavelength 730 nm) was delivered at a laser power of 20 mW as measured at the objective. To keep the laser power at the spine comparable over all experiments, only spines between 20 and 30 µm below the surface were considered. The glutamate-induced current at every spine was tested three times at each distance (Figure 4 and legend) and averaged to obtain an optimal signal-to-noise ratio. Igor Pro 7 (WaveMetrics) was used for all offline analyzes including the fitting of the uEPSCs obtained at 0 nm and 500 nm from the spine. Most uEPSCs were approximated with the custom-written fit function (adopted from Protopapas et al., 1998)

$$y(t) = y_0 + a \times (e^{-(t - onset)/decay} - e^{-(t - onset)/rise})$$

for  $t \ge onset$  and  $y(t) = y_0$  otherwise, with uEPSCs starting at t = onset and decay and rise referring to the decay and rise time constants, respectively. The amplitude was determined by evaluating y(t) at its maximum  $t_{\text{peak}} = \text{onset} + \ln(\text{decay}/\text{rise}) \times$  $(decay \times rise)/(decay - rise)$ . See Figure S4A for an example. In a few cases the decay of the uEPSC had to be fit with a monoexponential curve to obtain the decay time. An image stack (z steps of 1 μm) encompassing the recorded spine, the dendrite and nearby spines was obtained to analyze the spine volumes, as above (ExM).





It should be noted that the spatial resolution of both diffraction-limited two-photon excitation imaging and uncaging is insufficient to precisely mimic glutamate release from a presynaptic vesicle into the synaptic cleft. The initial spatial distribution of uncaged glutamate is determined by the uncaging point spread function (PSF), which is typically a few hundred nm wide in x-y and a multiple of that in z (Helmchen and Denk, 2005; Matsuzaki et al., 2001; Smith et al., 2003). When aiming at a spine surface, the PSF inevitably covers adjacent structures, visible or not, like spines and presynaptic boutons and the surrounding extracellular space, and the exact configuration changes from synapse to synapse. Therefore, the amount and extracellular distribution of glutamate uncaged into the extracellular space and the exact relative positions of spines, sampled NMDARs and uncaged glutamate will vary considerably from synapse to synapse, which could contribute to the variability of absolute uEPSC amplitudes (Figure S4). This also increases the variability of the attenuation of NMDAR-mediated currents. Therefore, the statistical relevance of the correlation between spine size and attenuation (Figure 4D) is an underestimate.

#### Glutamate iontophoresis and Ca2+ imaging

Ca<sup>2+</sup> imaging was performed as previously documented (Minge et al., 2017). Acute slices were transferred to a submersion-type recording chamber mounted on a Scientifica 2PE fluorescence microscope with a 40x/0.8 NA objective (Olympus), or a Olympus FV10MP 2PE fluorescence microscope with a 25x/1.05 NA objective, and superfused with ACSF at 34°C containing 10 μM NBQX, 1 μM TTX, 20 μM nifedipine, 50 μM LY341495, 10 μM MPEP. A CA1 pyramidal neuron was patched with a borosilicate glass pipette (3-4 MΩ resistance, using a Multiclamp 700B amplifier) with an intracellular solution containing (in mM): KCH<sub>3</sub>O<sub>3</sub>S 135, HEPES 10, di-Tris-Phosphocreatine 10, MgCl<sub>2</sub> 4, Na<sub>2</sub>-ATP 4, Na-GTP 0.4, Alexa Fluor 594 hydrazide 0.04 (to visualize the patched cell including its dendritic spines) and the Ca<sup>2+</sup>-sensitive fluorescent dye Fluo-4 0.2 (pH adjusted to 7.2 using KOH, 290-295 mOsm). Iontophoretic glutamate application was used to locally stimulate NMDARs at dendritic spines (MVCS-C-01C-150, NPI). The microiontophoretic pipette (60-80 M $\Omega$  resistance) was filled with 150 mM glutamic acid (pH adjusted to 7.0 with NaOH) and 50  $\mu$ M Alexa Fluor 594 hydrazide or Alexa Fluor 633 to localize the pipette. Patched cells with their dendritic spines and the microiontophoretic pipettes were visualized by 2PE imaging (wavelength 800 nm) and the microiontophoretic pipettes were brought in close proximity (~4 µm) to a dendritic segment. To avoid leakage of glutamic acid a small positive retain current (< 8 nA) was constantly applied. Neurons were held in the voltage clamp configuration at -70 mV. Recordings were discarded if the initial access resistance exceeded 16 MΩ or changed by more than 20% during the recording. The holding voltage was increased to -20 mV 30 s before iontophoretic glutamate application, to release the Mg<sup>2+</sup> block of NMDARs, and decreased back to −70 mV after four stimulation trials. The iontophoretic stimulation intensity (pulse duration < 0.7 ms, pulse intensity -0.5 to  $-0.9 \mu A$ ) was adjusted to obtain stable Fluo-4 fluorescence intensity transients using line scanning across multiple spines (~400 Hz, see Figure 5 for an illustration). Four baseline recordings were performed before 200 nM TFB-TBOA was bath-applied for at least eight minutes and another four recordings were obtained. In otherwise identical control experiments, TBOA was not added to the superfusion solution. In a subset of experiments 50 μM D-APV was washed in to confirm the NMDAR-dependence of the Fluo-4 response. For analysis, averages of the four baseline and four test trials were calculated and background-corrected. The Fluo-4 signal (F) was then normalized to the corresponding Alexa Fluor 594 signal (A) to obtain the ratio R = F/A. Responses to ionotophoretic glutamate application were further quantified by calculating the response's peak ratio ( $R_{MAX}$ ), the resting ratio before the stimulus ( $R_0$ ) and the response amplitude ( $\Delta R/R_0 = (R_{MAX}-R_0)/R_0$ ). The decay of responses was approximated by a monoexponentially decaying function. Spine volumes were determined from Alexa Fluor 594 image stacks (z-step 0.25 - 0.5 μm) as described above (ExM).

#### **QUANTIFICATION AND STATISTICAL ANALYSIS**

Image analysis was performed in FIJI/ImageJ (NIH), Huygens Essential (Scientific Volume Imaging), Elastix (https://doi.org/10.1109/ TMI.2009.2035616) and MATLAB (Mathworks). Numerical and statistical analysis was performed in Excel (Microsoft), Origin Pro (OriginLab Corporation) and MATLAB (Mathworks). In the text, results are given as mean ± standard error of the mean (SEM) unless stated otherwise. n denotes the number of experiments. In graphs, statistical significance is indicated by asterisks. \* for p < 0.05, \*\* for p < 0.01 and \*\*\* for p < 0.001. Paired and unpaired Student's t test and other analyses were used as appropriate and as indicated in the text and figure legends. All statistical tests were two-tailed. In some experiments, measurements at small and large spines on the same dendritic segment were compared (e.g., Figures 1 and 2). A paired statistical test was used in these cases, because measurements at small and large spines were obtained from the same sample. In other experiments, Spearman's rank correlation was used to analyze pooled data (Figures 3 and 4), because the number of spines per individual experiment/dendrite was sometimes low (Figure 3) or one (Figure 4). In these analyses, the volume of each spine was normalized to the median spine volume of the corresponding dendritic segment before pooling all data for statistical analysis using Spearman's rank correlation.